BAMS Article

Towards an End-to-End Analysis and Prediction System for Weather, Climate, and Marine Applications in the Red Sea

Ibrahim Hoteit, Yasser Abualnaja, Shehzad Afzal, Boujemaa Ait-El-Fquih, Triantaphyllos Akylas, Charls Antony, Clint Dawson, Khaled Asfahani, Robert J. Brewin, Luigi Cavaleri, Ivana Cerovecki, Bruce Cornuelle, Srinivas Desamsetti, Raju Attada, Hari Dasari, Jose Sanchez-Garrido, Lily Genevier, Mohamad El Gharamti, John A. Gittings, Elamurugu Gokul, Ganesh Gopalakrishnan, Daquan Guo, Bilel Hadri, Markus Hadwiger, Mohammed Abed Hammoud, Myrl Hendershott, Mohamad Hittawe, Ashok Karumuri, Omar Knio, Armin Köhl, Samuel Kortas, George Krokos, Ravi Kunchala, Leila Issa, Issam Lakkis, Sabique Langodan, Pierre Lermusiaux, Thang Luong, Jingyi Ma, Olivier Le Maitre, Matthew Mazloff, Samah El Mohtar, Vassilis P. Papadopoulos, Trevor Platt, Larry Pratt, Naila Raboudi, Marie-Fanny Racault, Dionysios E. Raitsos, Shanas Razak, Sivareddy Sanikommu, Shubha Sathyendranath, Sarantis Sofianos, Aneesh Subramanian, Rui Sun, Edriss Titi, Habib Toye, George Triantafyllou, Kostas Tsiaras, Panagiotis Vasou, Yesubabu Viswanadhapalli, Yixin Wang, Fengchao Yao, Peng Zhan, and George Zodiatis

ABSTRACT: The Red Sea, home to the second-longest coral reef system in the world, is a vital resource for the Kingdom of Saudi Arabia. The Red Sea provides 90% of the Kingdom's potable water by desalinization, supporting tourism, shipping, aquaculture, and fishing industries, which together contribute about 10%–20% of the country's GDP. All these activities, and those elsewhere in the Red Sea region, critically depend on oceanic and atmospheric conditions. At a time of mega-development projects along the Red Sea coast, and global warming, authorities are working on optimizing the harnessing of environmental resources, including renewable energy and rainwater harvesting. All these require high-resolution weather and climate information. Toward this end, we have undertaken a multipronged research and development activity in which we are developing an integrated data-driven regional coupled modeling system. The telescopically nested components include 5-km- to 600-m-resolution atmospheric models to address weather and climate challenges, 4-km- to 50-m-resolution ocean models with regional and coastal configurations to simulate and predict the general and mesoscale circulation, 4-km- to 100-m-resolution ecosystem models to simulate the biogeochemistry, and 1-km- to 50-m-resolution wave models. In addition, a complementary probabilistic transport modeling system predicts dispersion of contaminant plumes, oil spill, and marine ecosystem connectivity. Advanced ensemble data assimilation capabilities have also been implemented for accurate forecasting. Resulting achievements include significant advancement in our understanding of the regional circulation and its connection to the global climate, development, and validation of long-term Red Sea regional atmospheric–oceanic–wave reanalyses and forecasting capacities. These products are being extensively used by academia, government, and industry in various weather and marine studies and operations, environmental policies, renewable energy applications, impact assessment, flood forecasting, and more.

https://doi.org/10.1175/BAMS-D-19-0005.1
Corresponding author: Ibrahim Hoteit, ibrahim.hoteit@kaust.edu.sa
In final form 28 August 2020

AFFILIATIONS: Hoteit, Abualnaja, Afzal, Ait-El-Fquih, Antony, Attada, Dasari, Genevier, Gittings, Gokul, Guo, Hadri, Hadwiger, Hammoud, Hittawe, Knio, Kortas, Krokos, Langodan, Luong, Ma, El Mohtar, Raboudi, Razak, Sanikommu, Toye, Vasou, Wang, Yao, and Zhan—King Abdullah University of Science and Technology, Thuwal, Saudi Arabia; **Akylas and Lermusiaux**—Massachusetts Institute of Technology, Cambridge, Massachusetts; **Dawson**—The University of Texas at Austin, Austin, Texas; **Asfahani**—Saudi Aramco, Damam, Saudi Arabia; **Brewin**—University of Exeter, Cornwall, United Kingdom; **Cavaleri**—Institute of Marine Sciences, Venice, Italy; **Cerovecki, Cornuelle, Gopalakrishnan, Hendershott, Mazloff, and Sun**—Scripps Institution of Oceanography, La Jolla, California; **Desamsetti**—National Center for Medium Range Weather Forecasting, Noida, India; **Sanchez-Garrido**—University of Malaga, Malaga, Spain; **El Gharamti**—National Center of Atmospheric Research, Boulder, Colorado; **Karumuri**—University of Hyderabad, Hyderabad, India; **Köhl**—University of Hamburg, Hamburg, Germany; **Kunchala**—Indian Institute of Technology, Delhi, India; **Issa**—Lebanese American University, Beirut, Lebanon; **Lakkis**—American University of Beirut, Beirut, Lebanon; **Le Maitre**—Ecole Polytechnique, Palaiseau, France; **Papadopoulos, Triantafyllou, and Tsiaras**—Hellenic Centre for Marine Research, Anavissos, Greece; **Platt,* Racault, and Sathyendranath**—Plymouth Marine Laboratory, Plymouth, United Kingdom; **Pratt**—Woods Hole Oceanographic Institution, Woods Hole, Massachusetts; **Raitsos and Sofianos**—National and Kapodistrian University of Athens, Athens, Greece; **Subramanian**—University of Colorado Boulder, Boulder, Colorado; **Titi**—University of Cambridge, Cambridge, United Kingdom, and Texas A&M University, College Station, Texas; **Viswanadhapalli**—National Atmospheric Research Laboratories, Gadanki, India; **Zodiatis**—Coastal and Marine Research Laboratory, Crete, Greece
*** Deceased.**

The Red Sea is a semi-enclosed, elongated marginal sea, lying between Africa and Asia, connected to the Indian Ocean through the Strait of Bab-al-Mandeb (BaM; see Table A1 in the appendix for a full list of acronyms and abbreviations used in the paper) in the south and to the Mediterranean Sea through the Suez Canal in the north (Fig. 1). As a vital resource for fisheries, agriculture, tourism, and freshwater through desalination and as a major shipping route, the Red Sea is of paramount political and economic importance for both the region and the world. Influenced by distinct geological, atmospheric, and hydrographic conditions, the Red Sea is a unique LME characterized by the second-longest and third-largest coral reef system in the world, thriving under one of the warmest and most saline conditions of the world oceans (Edwards and Head 1987). All major oceanographic processes occur in the Red Sea, but at much smaller spatiotemporal scales compared to the global ocean, making it an ideal test basin for studies of climate impact on regional ocean circulations as it is expected to exhibit a faster response to global climate variations (Belkin 2009; Carvalho et al. 2018). Despite its political, economic, and scientific importance, the Red Sea remains a vastly underexplored region.

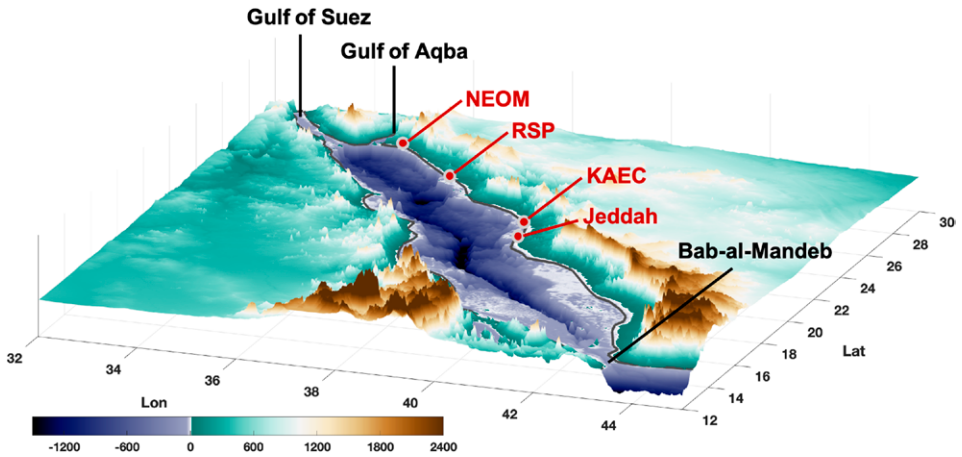

Fig. 1. Topography of the Red Sea region. The important sites along the Saudi coastline are indicated on the map.

The Red Sea is a geologically young ocean with an average width of 280 km, length of 2,000 km, and maximum depths exceeding

2,500 m along its axial trench. Extending from 12.5° to 30°N in the northwest–southeast direction, it has a constricted connection with the Gulf of Aden, with a maximum depth of only 137 m at the Hanish Sill. The bathymetry varies from extensive shallow shelves with depths <50 m in the south to steep-sloped basins with depths >800 m in the north.

The atmospheric conditions over the Red Sea are mainly influenced by the arid surrounding terrestrial environment, the seasonal Indian monsoon system, and the orographic effects of the coastal mountains, with the resultant atmospheric forcing exhibiting marked variability on various time scales (Viswanadhapalli et al. 2017). As a result of the arid climate, the annual mean net freshwater loss due to excess of evaporation over precipitation is estimated at ~2 m yr^{-1}, and the heat flux has a relatively small annual mean heat loss of 11 W m^{-2}, but a large annual cycle with a range of ~200 W m^{-2}. Channeled by the coastal mountains, the surface winds tend to follow the direction of the axis of the Red Sea. In summer (June–September) they generally blow from northwest throughout the whole basin, whereas in winter they reverse from southeast to northwest in the southern Red Sea, creating a convergence zone around 18°N (Langodan et al. 2014, 2017a). On smaller spatial scales, intense across-basin winds flowing between the coastal mountain gaps are also observed, the most prominent of which is the Tokar jet at around 18°N of the African coast. This jet is known to generate surface eddies in the Red Sea (Zhai and Bower 2013; Zhan et al. 2018) and to gather moisture from the surface of the Red Sea that can contribute to precipitation over Saudi Arabia and the African Highlands region (Davis et al. 2015; Dasari et al. 2017). North of 20°N, the mountain-gap winds usually originate from the Arabian subcontinent and blow westward.

In response to the atmospheric forcing and limited exchanges with the Indian Ocean (Pratt et al. 2000), the Red Sea acts as a concentration basin, producing one of the world's saltiest water masses through a complex two-layer overturning system (Fig. 2). In annual mean, an overturning cell occupies the upper layer around the sill depth in the south and deepens to about 300 m in the north. It is composed of a northward surface inflow from the Gulf of Aden and an intermediate southward flow (Sofianos and Johns 2007). This layer is directly subject to the annual cycle of surface heat flux and freshwater loss, resulting in marked seasonal surface temperature variations and a northward increase in surface salinity (Sofianos and Johns 2015). The Red Sea intermediate water is formed in the north during winter and is exported into the Gulf of Aden through BaM, driving a two-layer water exchange (Sofianos and Johns 2007; Zhai et al. 2015). During summer, the above overturning circulation and water exchange in the strait reverse, following the onset of the Indian summer monsoon (Yao et al. 2014a,b). An intermediate water intrusion at depths 50–100 m is induced from the Gulf of Aden, the mean surface currents change to flow southward, and the water exchange in BaM becomes a three-layer structure with the deep outflow significantly suppressed (Patzert 1974; Smeed 1997). The lower layer of the overturning system, extending to the basin bottom, is occupied by a nearly homogeneous warm (~21.5°C) and highly saline (~40.5 psu) water mass, referred to as the RSDW. A deep circulation with a southward bottom flow and an intermediate northward return flow centered around a depth of 500 m is suggested by geochemical tracers and dissolved oxygen gradients (Cember 1988; Eshel et al. 1994).

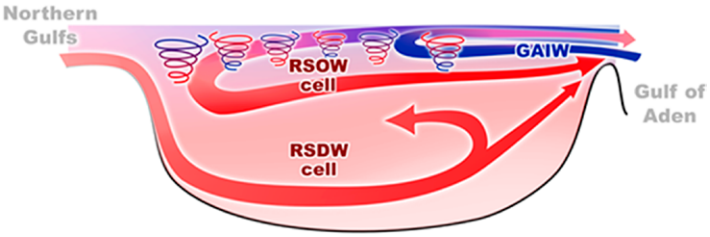

Fig. 2. Schematic representation of the main thermohaline cells in the Red Sea circulation (Carvalho et al. 2018). Blue colors represent fresher water while red colors saline and denser water masses. Mesoscale features (cyclonic and anticyclonic eddies) are represented by spirals. RSOW, RSDW, and GAIW stand the for Red Sea Outflow Water, Red Sea Deep Water, and Gulf of Aden Intrusion Water, respectively.

Despite being characterized as an oligotrophic LME, the Red Sea is a region of remarkable biodiversity and endemism and hosts one of the world's largest coral reef ecosystems (Carvalho et al. 2018). The Red Sea ecosystem is strongly influenced by environmental conditions, which modulate it on different levels (Triantafyllou et al. 2014). The Red Sea has been subject to warming trends (Raitsos et al. 2011; Chaidez et al. 2017; Krokos et al. 2019), causing coral reef bleaching events (Cantin et al. 2010; Osman et al. 2018; Genevier et al. 2019) and significantly impacting its productivity (Raitsos et al. 2015; Gittings et al. 2018). The Red Sea ecosystem, with its relatively simply shaped and semi-enclosed basin, high biodiversity, and rich dynamics, provides the scientific community with an accessible and ideal natural laboratory to study the physical–biological interactions on multiple spatial and temporal scales.

Until recently, the Red Sea region remained largely underdeveloped. The last decade has, however, witnessed an unprecedented increase in population and an acceleration in residential, commercial and industrial developments along the coast. NEOM, short for the Latin–Arabic term Neo-Mustaqbal, signifying "new future," is a $500 billion mega-project that aims at building a fully automated city operating as an independent economic zone in the northwestern part of Saudi Arabia. The RSP is another mega-development along the central Saudi coast and intends to transform the Red Sea coast into a world-class tourist destination, whose blueprint is primarily based on a coastal lagoon with 90+ pristine islands.

Maintaining a sustainable, healthy marine environment is a core objective of these developments and the Saudi authorities. In this context, understanding and forecasting the regional weather through climate variations is essential for a wide variety of high-impact societal needs, including environmental protection and coastal management, mitigating weather extremes and pollution/contamination, exploration and drilling, accidents response, desalination and plant cooling operations, shipping, harbor management and national security operations, management of fisheries and marine aquaculture, water resources, and renewable energy. Given the unique structure of the Red Sea basin and surrounding deserts, and the ocean and atmospheric connections to the global circulation, the need for integrated state-of-the-art modeling and supporting datasets is acute.

Founded in 2009 and located on the shores of the Red Sea, KAUST acts as a hub of frontline research in the biological, physical, and geological aspects of the Red Sea region. For this purpose, KAUST dedicated significant resources for studying the Red Sea and understanding its resources, with the goal of preserving its fragile ecosystem while at the same time supporting the local authorities to exploit its unique resources. In parallel to the ongoing hydrographic and ecological observational efforts, and through sustained and strong collaborations with many international organizations, the Red Sea Modeling and Prediction group at KAUST has led the development of a comprehensive and integrated modeling and prediction system to study, monitor, and predict the atmospheric and oceanic phenomena of the region. The system is being built by integrating models of atmospheric and oceanic circulations, surface wave, air pollution, dust, and marine biogeochemistry, and developing advanced data analytics and visualization capabilities, achieving remarkable progress in the short span of a decade. The modeling system also relies on in situ and remotely sensed observations (detailed in Table 1) for the purpose of validation and data assimilation and provides insights into the systematic relations between the interactions of different components and the management of various applications.

An important achievement from this effort is the first high-resolution atmospheric reanalysis for the region from 1980 to the present, generated using our assimilative atmospheric modeling system, which is turning out to be critical not only for the Red Sea climate research, but also contributing to Indian monsoon studies. This regional reanalysis is being used to force the various ocean and transport models tuned to the Red Sea environment. Notably, these capabilities are currently being extensively used to support various industrial and governmental

Table 1. A variety of in situ and satellite observations and reanalysis datasets are being used to study the regional ocean and atmospheric variabilities and changes, to validate our models, for prescribing model boundary conditions, and for initialization and assimilation. We have also developed regionally tuned remote sensing algorithms, based on local observations, to generate improved chlorophyll datasets for the Red Sea region (Brewin et al. 2019). Details of the datasets and their use are listed here.

Datasets and observations	Type	Usage
Atmospheric datasets		
ERA-Interim, NCEP FNL, real-time global SST, CCMP, CRU	Reanalyses	Initialization and boundaries
AMSU, QuikSCAT, ASCAT, GPSRO	Satellite	
TRMM, CMORPH, APHRODITE	Rainfall reanalysis	Model validation
Rain gauge precipitation, AWS–PME, KSA	Local	Assimilation and validation
Saudi Aramco, KSA	Met-ocean	
RADAR, PME, KSA		
KAUST–WHOI buoy		
Synoptic and upper—University of Wyoming		
GlobWave altimeter wave data	Significant wave height	Wave model validation
Oceanic datasets		
ECCO2, WOA, GLORYS2	Reanalyses	Initialization and boundaries
AVHRR, RADS	Satellite	Assimilation and validation
RSP, NEOM, Saudi Aramco Tidal Gauges, KAUST-WHOI buoy	In situ observations	Model validation
OSTIA, AVISO	Satellite	
OTIS	Simulation	Tidal forcing
ESA: Ocean Color Climate Change Initiative (OC-CCI) and *Sentinel-3* OLCI	Satellite	Ocean color/ecological indicators

developments. This review paper elaborates on our state-of-the-art modeling and forecasting technologies, their applications, achievements in science, and contributions to industry. It first provides a detailed description of our integrated data-driven Red Sea Modeling system, version 1 (iReds-M1). It then catalogues some of our salient science findings and industrial applications using iReds-M1 simulations. It finally lays down our vision for the future development of the system and research directions.

The Integrated Red Sea Model (iReds-M1)

iReds-M1 is a comprehensive system comprising a set of state-of-the-art modeling components for simulating the atmosphere, ocean, waves, transports, and biogeochemistry (as schematized in Fig. 3). In its present form, the WRF Model is used to force various ocean and transport models. The regional ocean and wave models, based on the MITgcm and WWIII, were further recently fully coupled with WRF (Sun et al. 2019). These regional models are further used to force transport models and to nest very high-resolution coastal ocean models. The system is implemented on the Shaheen-II Cray XC40 supercomputer at KAUST, a 36-cabinet Cray composed of 6,174 dual-socket compute nodes based on 16 core Intel Xeon E5-2698v3 processors running at 2.3 GHz, capable of delivering a theoretical peak of 7.2 PFLOP s^{-1} (Hadri et al. 2015). A description of the components follows.

The atmospheric models. WRF is a state-of-the-art mesoscale model offering numerous advanced physics options for simulating atmospheric processes at various scales, providing a robust and flexible platform for assimilation (Skamarock et al. 2019). In various baseline studies, WRF successfully reproduced the mean regional climate of the AP and its

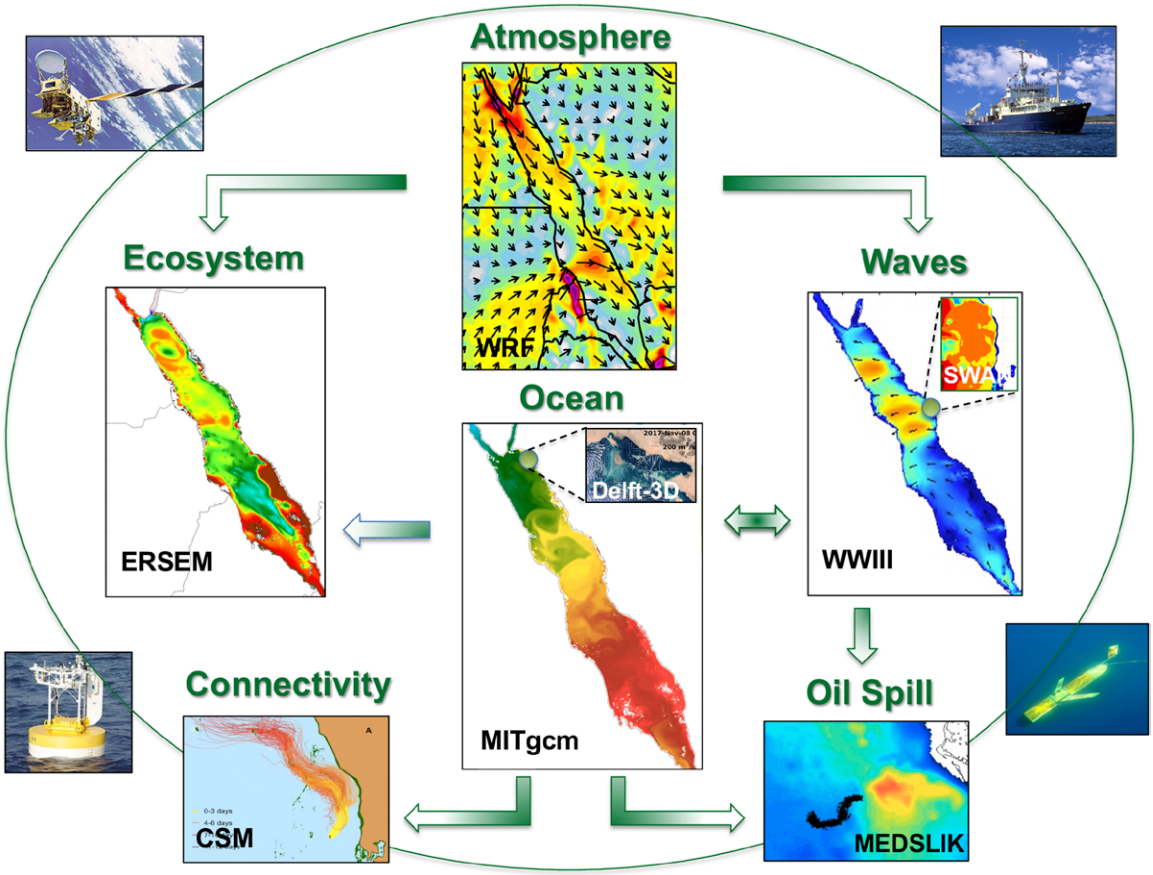

Fig. 3. Schematic illustration of the data-driven Red Sea modeling and prediction system (iReds-M1). Two-way arrows signify two-way coupling, and one-way arrows represent forcing of uncoupled components. The atmosphere panel shows mean wind speeds during the month of July from 5-km WRF Red Sea reanalysis. The ocean panel shows a sea surface temperature snapshot in September with the upper-corner subpanel displaying the volume transport in the upper layer of a high-resolution coastal nesting exercise in the NEOM region. The ecosystem panel shows the simulated near-surface Chl-a during the winter-mixing period (January–March). The waves panel shows a significant wave heights and mean wave directions snapshot in January with the upper-corner subpanel displaying the distribution of maximum significant wave heights estimated from a high-resolution nested coastal model long run covering the KAEC region. The connectivity and oil spill panels show simulations of oil and virtual larvae trajectories released in the central Red Sea.

interannual variability (Viswanadhapalli et al. 2017). It also accurately delineated the structure and climatology of the monsoon low-level jet and monsoon inversion over the Arabian Sea (Viswanadhapalli et al. 2020). We further used long-term WRF simulations to carry out detailed assessments of renewable energy resources in the AP (Langodan et al. 2016a; Dasari et al. 2019) and for analyzing extreme events (e.g., Viswanadhapalli et al. 2016).

We have implemented WRF in assimilation mode at 5-km resolution using the ECMWF global reanalysis as initial and boundary conditions to generate the first high-resolution regional reanalysis for the region from 1980 to the present (Viswanadhapalli et al. 2017; Langodan et al. 2017a,b). Available satellite and conventional observations in the AP were assimilated (Fig. 4). The reanalysis fields are being used to study, for instance, the regional meteorology–ocean (met-ocean) conditions (e.g., Viswanadhapalli et al. 2017, 2020), to provide vital information about the background state of the regional environment (e.g., Dasari et al. 2020), and to force our regional ocean models (e.g., Langodan et al. 2014, 2016a; Zhan et al. 2019; Krokos et al. 2021, manuscript submitted to *J. Geophys. Res. Oceans*).

To simulate air parcel trajectories as well as transport, dispersion, chemical transformation, and deposition, we use HYSPLIT (Draxler and Hess 1997). HYSPLIT, forced with specially

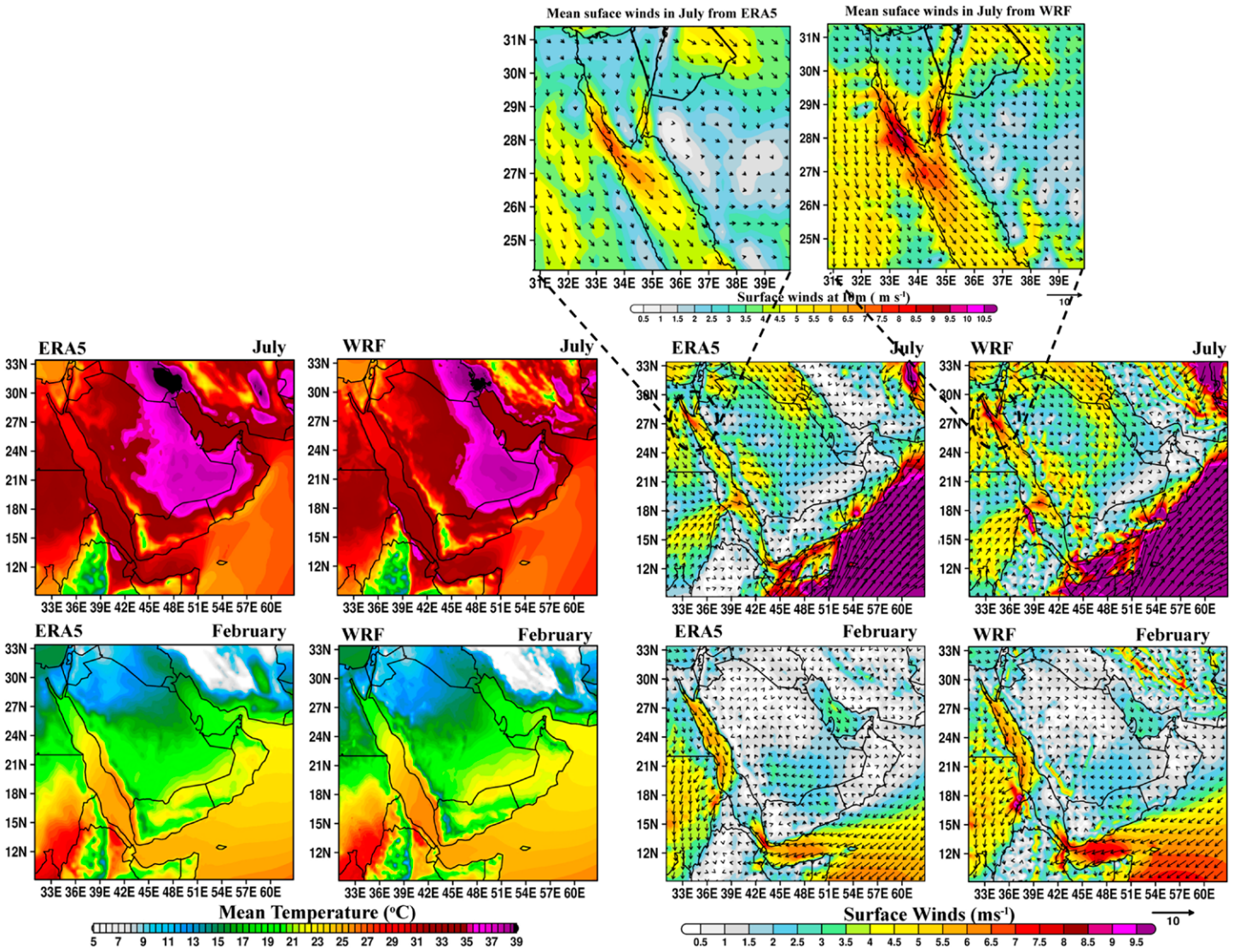

Fig. 4. The spatial distribution of (middle) summer (July) and (bottom) winter (February) months climatology of air temperature at 2-m height, and winds at 10-m height from the 5-km Red Sea reanalysis compared against ERA5. The Red Sea reanalysis reproduces well the main regional winds features in summer and winter, in good agreement with ERA5. (top) Zoomed-in views over the northern Red Sea region to emphasize the wind features captured by the high-resolution Red Sea reanalysis winds.

generated WRF forcing at 600-m resolution, was recently used to investigate the distributions of air pollutant concentrations at sites along the Red Sea coast, including the NEOM and RSP regions (Dasari et al. 2020).

The ocean models. The regional Red Sea circulation is simulated using a 1-km resolution MITgcm (Marshall et al. 1997a,b). The model domain covers the entire Red Sea including the two gulfs (Suez and Aqaba) at the north end, with an open boundary in the Gulf of Aden. The model topography is generated based on the General Bathymetric Chart of the Ocean (IOC et al. 2003), updated with available regional data. The eastern open boundary conditions are extracted daily from the global ocean reanalysis GLORYS2. To resolve the different frequencies of water elevation variations (Churchill et al. 2018), the normal velocity at the boundary is adjusted to match the volume flux of GLORYS2. The model is forced with hourly high-resolution WRF downscaled fields, including surface wind, air temperature, specific humidity, precipitation, and downward shortwave and longwave radiation. The Red Sea MITgcm outputs were validated against different datasets and in various settings and applications

(Fig. 5). These include studying the general and overturning circulation (Yao et al. 2014a,b), mixed layer variations (Krokos et al. 2020, manuscript submitted to *J. Geophys. Res. Oceans*), deep-water formation events (Yao and Hoteit 2018), eddy characteristics (Zhan et al. 2016, 2019), and internal/baroclinic tides (Guo et al. 2018). In addition, the adjoint model of MITgcm is being used to conduct sensitivity studies of quantities of interest with respect to the model states and atmospheric forcings (Zhan et al. 2018).

WWIII (Tolman 2008) is used to simulate the waves conditions in the Red Sea at 1-km resolution. The model is configured with 33 frequencies, starting from 0.05 Hz and 36 equally spaced directions and the most recent (ST4) physics formulation (Ardhuin et al. 2010). The extensively validated model outputs (Langodan et al. 2014) were analyzed to assess the impact of atmospheric data assimilation on wave predictions (Langodan et al. 2016b), to investigate

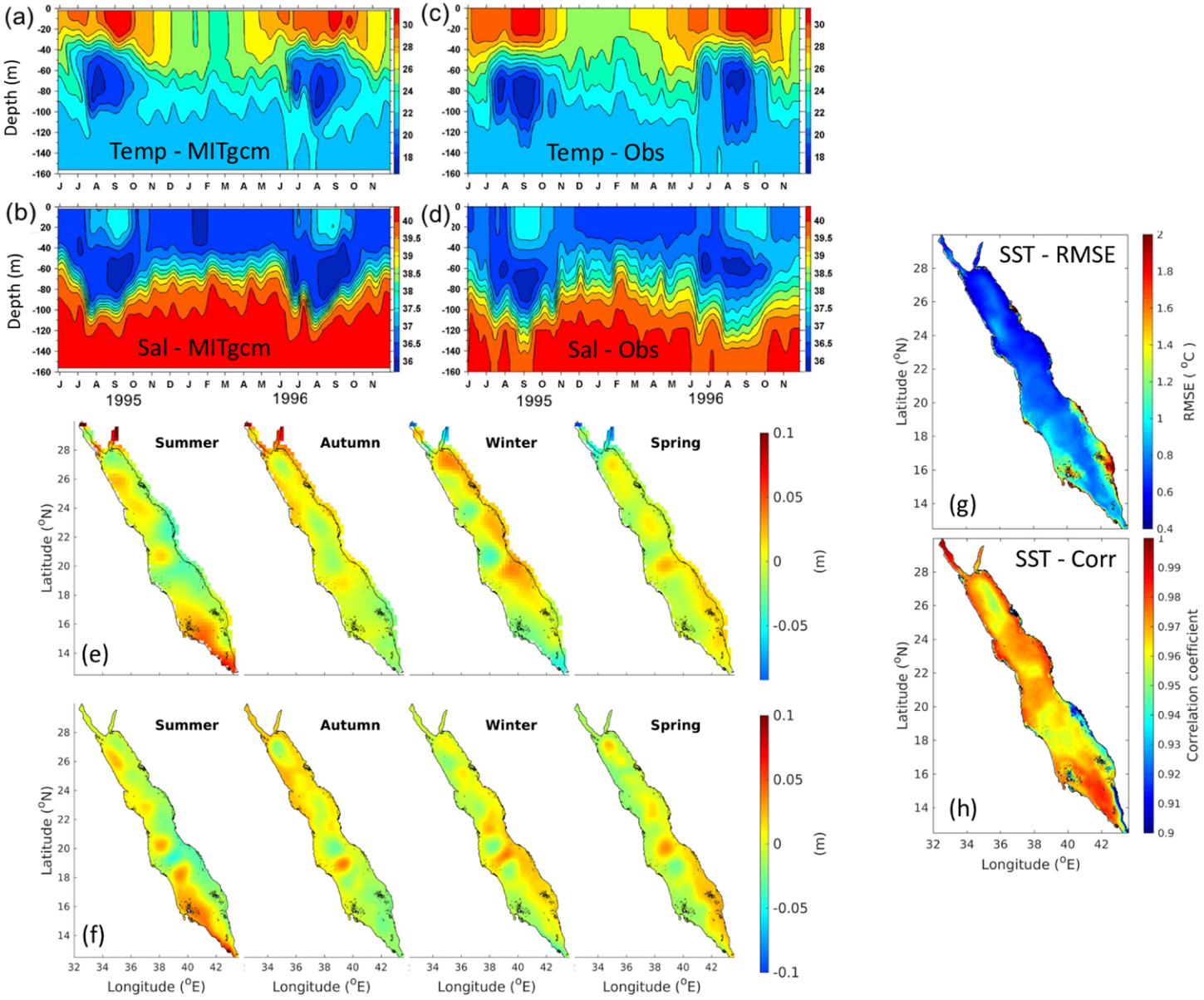

Fig. 5. (a)–(d) Hovmöller diagrams (time vs water depth) of (a),(c) temperature (°C) and (b),(d) salinity (psu) at the Hanish Sill, from June 1995 to November 1996, after filtering with a 20-day low-pass filter. (a),(b) 400-m-resolution southern Red Sea MITgcm simulations taken from Xie et al. (2019) and (c),(d) in situ observations. (e),(f) Seasonal climatology of sea level anomaly derived from (e) satellite altimetry data (AVISO) and (f) 1-km MITgcm for the period 2001–15, in summer (June–August), autumn (September–November), winter (December–February), and spring (March–May). (g) RMSE and (h) correlation coefficient between satellite derived SST (OSTIA) and 1-km daily MITgcm SST, time averaged over the model simulation period of 2001–15. MITgcm successfully reproduces the main features of the general circulation of the Red Sea.

the physical aspects of the unique seasonally opposing wind-wave systems in the central Red Sea (Langodan et al. 2015), to quantify wave energy potentials (Langodan et al. 2016a), and to study the wind-wave climate and its trends (Langodan et al. 2017a,b, 2018, 2020a).

Transport phenomena are simulated using CMS, a multiscale probabilistic model of particle dispersal (Paris et al. 2013). CMS, driven by the MITgcm flow fields, has been successfully implemented to study concentrate discharges (Zhan et al. 2015), biological connectivity among different coral reef complexes at coastal (Nanninga et al. 2015), basin (Raitsos et al. 2017), and cross-basin scales (Wang et al. 2019). Oil spill transport and weathering processes are simulated with the well-established MEDSLIK oil spill, trajectory, and pollutant transport prediction model (De Dominicis et al. 2013a,b; http://www.oceanography.ucy.ac.cy/medslik/) as Lagrangian particles transported by ocean currents, wind, and waves, and a stochastic displacement that parameterizes turbulent diffusion (Zodiatis et al. 2019).

The marine biogeochemical cycle is simulated using ERSEM (Baretta et al. 1995). ERSEM is a generic comprehensive model that has been successfully implemented across a wide range of coastal and open-ocean ecosystems (e.g., Petihakis et al. 2002; Collingridge 2012). It is based on a "functional" group approach, using size as the major biotic group characteristic. The pelagic model food web consists of four phytoplankton groups, bacteria, and three zooplankton groups, and is coupled with the associated benthic model that includes the settling of organic detritus into the benthos and diffusional nutrient fluxes out of the sediment. The pelagic variables include particulate and dissolved organic matter, along with dissolved inorganic nutrients, allowing the coupling of biologically driven carbon dynamics with the chemical dynamics. ERSEM forced with the outputs of our MITgcm and WRF model outputs has been successfully implemented by Triantafyllou et al. (2014) to describe the main seasonal features of the Red Sea ecosystem.

To simulate complex coastal processes, we implemented ocean models specifically designed for coastal and engineering applications at very high resolutions on the order of 10 m. These include (i) the Delft3D model (Deltares 2016) to simulate coastal circulation, including flow induced by tides and wind, and sediment transport, (ii) the shallow-water ADCIRC model (Luettich and Westerink 2004) to simulate water level variations and surges on an unstructured grid that enables resolution of near-shoreline detail, and (iii) the SWAN model (Booij et al. 1999) that is coupled with both Delft3D and ADCIRC and designed for simulating short crested waves in coastal environments. These models are forced with high-resolution downscaled WRF fields and are nested within the regional MITgcm and WWIII models.

Coupled ocean–atmosphere modeling. Ocean temperatures over the Red Sea region play an important role in modulating the region's weather and climate (Gimeno et al. 2010; Sun et al. 2019). Furthermore, while most of the AP experiences hot and dry summers, the conditions in coastal regions east of the Red Sea are relatively cooler and humid owing to transported moisture from the Red Sea. SKRIPS is a new regional coupled ocean–atmosphere WRF + MITgcm + WWIII system that was developed as part of iReds-M1 to study air–sea feedbacks in the Red Sea region and to build long-term regional forecasting capabilities (Sun et al. 2019). Coupling between these components is based on ESMF (Hill et al. 2004) and the interfaces are implemented according to the NUOPC consortium. This regional coupled model allows for oceanic mixed layer heat and momentum to interact with the atmospheric boundary layer dynamics at the mesoscale and higher resolution. This should reproduce feedbacks that cannot be well resolved by coarse-resolution global coupled models and are absent in regional uncoupled models. SKRIPS was used to investigate the heatwaves in the Red Sea region on seasonal scales, demonstrating that the evolving ocean temperatures considerably improve the prediction of the amplitude of these heatwaves (Fig. 6), particularly in the coastal region (Sun et al. 2019).

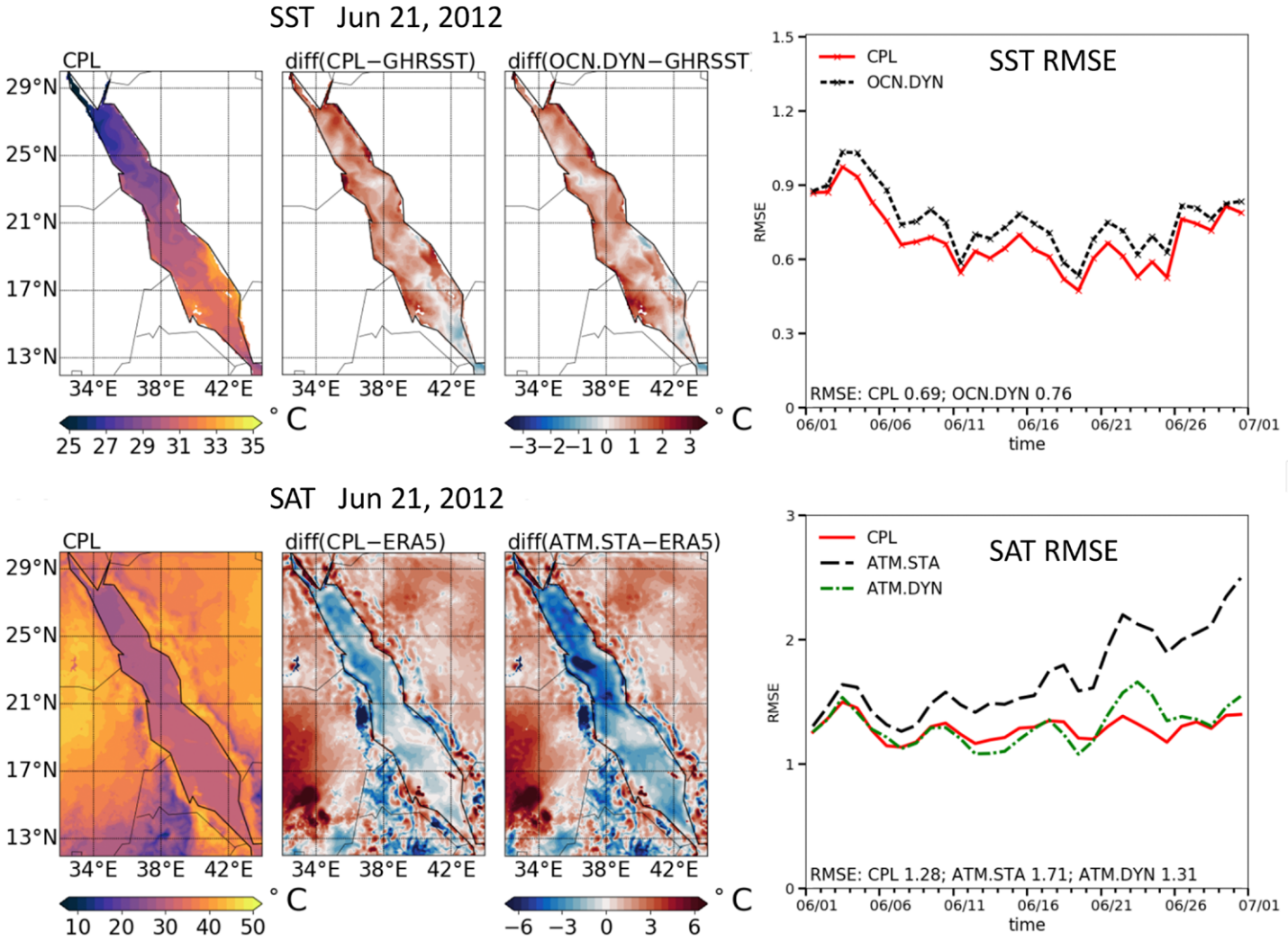

Fig. 6. Validation results for (top) SST and (bottom) surface air temperature (SAT), as simulated by the coupled SKRIPS model (Sun et al. 2019). CPL, OCN.DYN, ATM.STA, and ATM.DYN denote the coupled WRF–MITgcm run, MITgcm-only driven by ERA5, WRF-only run driven by persistent HYCOM SST, and WRF-only run driven by time-varying HYCOM SST, respectively. SST is compared against GHRSST and SAT is compared against ERA5. The simulation initial time is 0000 UTC 1 Jun 2012 for all runs. Coupled and uncoupled runs well simulate SST and SAT in the Red Sea region with smaller RMSEs from the coupled simulation compared to the validation data.

Data assimilation. Assimilation is a process by which a model is constrained toward available observations to obtain improved forecasts/hindcasts (Edwards et al. 2015; Hoteit et al. 2018). Our atmospheric and ocean general circulation models are equipped with state-of-the-art assimilation packages: DART (Hoteit et al. 2013), which comprises advanced ensemble schemes (Anderson et al. 2009) and the adjoint-based ECCO-4DVAR system (Stammer et al. 2002; Hoteit et al. 2006) for MITgcm, and the extensive assimilation package of WRF (Barker et al. 2012), which also includes DART. We are currently employing a cyclic 3DVAR for assimilation with WRF (Viswanadhapalli et al. 2017) and an ensemble adjustment Kalman filter (EAKF) for MITgcm (Toye et al. 2017, 2018). We have recently further developed the DART–MITgcm system to operate with hybrid ensembles composed of flow-dependent and seasonally varying static members (Toye et al. 2020) and demonstrated significant improvements when driving the MITgcm with ensembles of forcing and physics (Sivareddy et al. 2020). We are currently working on tuning DART for WRF and on testing newly introduced ensemble assimilation schemes (Hoteit et al. 2015; Raboudi et al. 2018). The system is being further equipped with new efficient techniques for simulating transport

phenomena (El-Mohtar et al. 2018) and control of unmanned vehicles (Wang et al. 2016; Albarakati et al. 2019) under the uncertainties described by the ensembles.

We assimilate a variety of observations from different networks, including satellite (e.g., altimeter SSH and AVHRR SST in the ocean, and QuikSCAT and Advanced Scatterometer winds in the atmosphere) and land-based remote sensing (e.g., weather radars), station-based (e.g., oceanic temperature and salinity observations from moored buoys and ships, meteorological observations from synoptic stations and METAR) and freely drifting (e.g., Argo observations in the ocean and upper-air soundings of rawinsonde and pilot balloon) in situ observations. Figure 7 demonstrates the important improvement achieved after ocean assimilation, with significant reduction in the SST and SSH biases in the Red Sea and Gulf of Aden compared to the model free run. On average, assimilation reduced the forecast RMSEs by 0.5°C for SST and 3 cm for SSH. The assimilated ocean solution is closer to both SST and SSH observations than the corresponding interpolated level-4 products. An operational system for the Red Sea is currently being developed based on a hybrid ensemble assimilation scheme as part of a project with Saudi Aramco.

Visualization and data analytics. Advanced visualization is an integral component of our system to support data analysis tasks for scientists and nonexpert users. We have developed a visual analytics application, called RedSeaAtlas (Afzal et al. 2019a), considering the tasks and computational and operational requirements of the variety of simulation models and

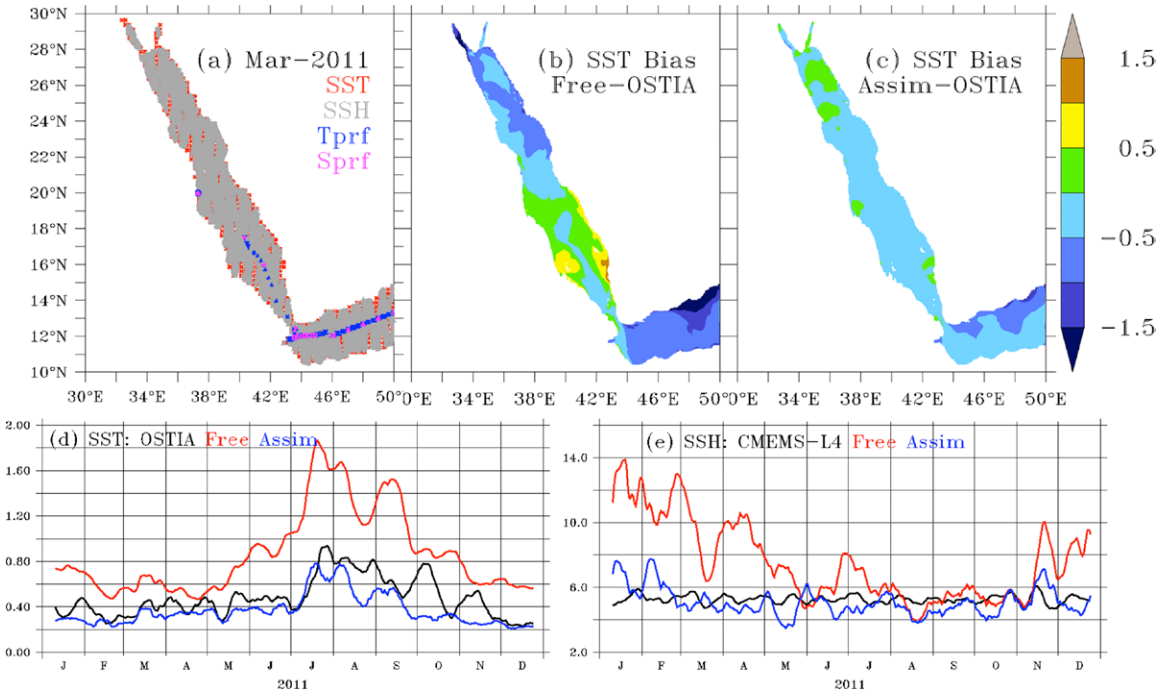

Fig. 7. Impact of assimilation in the ensemble DART–MITgcm assimilation system. (a) The spatial distribution of SST, SSH, and in situ temperature and salinity observations that were assimilated in the DART–MITgcm ocean ensemble system during an arbitrary month (March 2011). The coverage of the regularly spaced SST observations (red dots) is mostly masked by that of along-track SSH (gray dots) observations, which cover most of the Red Sea basin over a 1-month period. The SST bias for (b) free- and (c) assimilative-model runs estimated over the period 1 Mar–31 Dec 2011 with respect to OSTIA, a 5-km-resolution daily available interpolated level-4 gridded product generated by blending satellite and in situ observations of SST. Also shown are the time series of forecast RMSEs averaged over the model domain for (d) SST (°C) and (e) SSH (cm). Black, red, and blue curves correspond to RMSEs of OSTIA for SST and CMEMS-L4 for SSH (available daily at 25-km resolution), and free- and assimilative-model runs, respectively.

observational datasets of the Red Sea region. The application provides a suite of visualization tools that can facilitate diverse research tasks through interactive visual exploration and analysis of spatiotemporal multivariate data (Fig. 8). These include interactive feature selection, spatial and temporal filtering, overview and details on demand, and capability to analyze data from disparate data sources (Afzal et al. 2019b).

We have also developed an interactive visual analysis framework, called Ovis (Höllt et al. 2013, 2014), for interactive exploration and analysis of ensemble data. The core components of this framework are constructed based upon an efficient GPU-based computation and visualization pipeline. We presented two case studies to showcase the effectiveness of this framework: the first investigated the placement planning and operation of offshore structures related to oil and gas industry, and the second demonstrated the effectiveness of this system to plan pathways of autonomous sea vehicles (gliders) through interactive exploration and analysis of ensemble data (Höllt et al. 2013, 2015).

iReds salient contributions to science and industry

Study of the Red Sea region circulation, climate, and ecosystem.

Atmospheric variability. Motivated by the background knowledge from the analysis of global fields, and to meet the need for high-resolution datasets to resolve mesoscale characteristics, we developed a regional reanalysis at 5-km resolution for a 39-yr (1980–2018) period (wind details captured by this regional reanalysis are illustrated in Fig. 4). The reanalysis fields accurately reproduced the known regional climatic features such as the Red Sea Trough, Red Sea Convergence Zone, Arabian anticyclone, and seasonal circulation patterns (Viswanadhapalli et al. 2017). It has been further extensively used to drive iReds ocean models and for subsequent regional applications, and to support the mega-projects being developed along the Red Sea coast. Several studies were also conducted using convective-permitting WRF configurations to investigate the predictability of extreme rainfall over the Mecca region, discussed more in detail below.

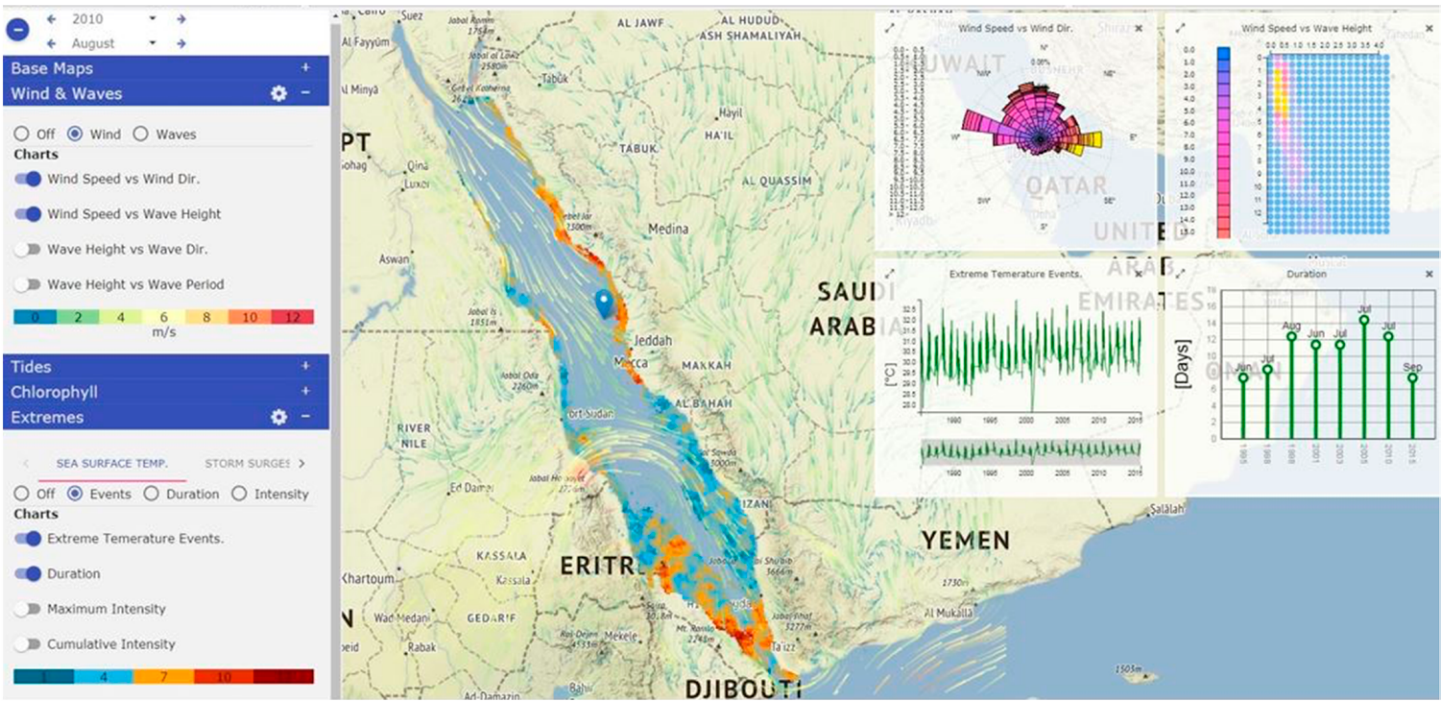

Fig. 8. The RedSeaAtlas system showing overall wind patterns and statistics (at the dropped pin location, here north of Jeddah in the central Red Sea) of extreme temperature events in the Red Sea. Users can select any region to show more detailed information and associated attributes through different charts (Afzal et al. 2019b).

Based on global reanalyses, our study of the regional surface air temperature suggested that it is strongly modulated by the circulation patterns (Attada et al. 2018a,b), and demonstrated an impact of the Indian summer monsoon through westward-propagating Rossby waves (Attada et al. 2018c). Dasari et al. (2018) and Dasari et al. (2021, manuscript submitted to *J. Climate*) showed that the baroclinic instability induced by the intensification and southward shift of the subtropical westerly jet over the AP facilitates an increase in the passage of synoptic transients and winter rainfall. Kunchala et al. (2018, 2019) showed a significant increasing trend in the recent decade in the summer AOD over AP, related to an intensification of the Tokar jet.

Ocean general circulation. The Red Sea MITgcm has provided an unprecedented description of the 3D basin circulation and its seasonal and interannual variability. The local buoyancy forcing and Indian monsoon seasonally reverse the basin overturning circulation, and ultimately modulate the water exchanges with the Gulf of Aden through BaM (Yao et al. 2014a,b). Analysis of the interannual variability of the exchanges based on long-term MITgcm simulations forced with the in-house high-resolution regional Red Sea reanalysis further demonstrated a strong dependence on the intensity and duration of the Indian monsoon (Raitsos et al. 2015; Dreano et al. 2016; Xie et al. 2019). Such simulations also revealed the episodic nature of deep-water renewal related to specific atmospheric events and provided updated estimates of the deep-water renewal time Yao and Hoteit (2018). A 1-km model simulation together was recently analyzed to provide a detailed description of the seasonal and spatial variability of the Red Sea mixed layers (Krokos et al. 2020, manuscript submitted to *J. Geophys. Res. Oceans*). The study revealed the dominant role of the air–sea heat fluxes on the mixed layers seasonal variability and the north–south gradient while the effects of extreme evaporation mainly manifest on interannual time scales.

MITgcm–ERSEM–CMS simulations, combined with various remote sensing datasets, have provided new insights into the manner in which physical drivers such as buoyancy fluxes and ocean mixing, and biogeochemical processes drive the ecosystem in the Red Sea. Despite a limited supply of nutrients, their subsurface intrusion from the Gulf of Aden and the winter deep convection drive elevated values of primary productivity in the south during summer (Raitsos et al. 2013; Dreano et al. 2016) and in the north during winter (Gittings et al. 2018). Moreover, marine larvae/planulae disperse nearly passively with the circulation, forming a homogeneous genetic connectivity across geographically separated reef sites within most of the basin (Fig. 9; Raitsos et al. 2017), except for the southern Red Sea, which was suggested to be physically connected with the Indian Ocean (Wang et al. 2019).

Mesoscale circulation. The upper-layer Red Sea circulation is characterized by complex and highly varying mesoscale activity, consisting of energetic semipermanent and transient eddies, with stronger activity during winter (Zhan et al. 2014). Spatially, the central and northern regions show annual eddy kinetic energy (EKE) peaks during both seasons, with effects on the water column reaching down to 300 m and intensified toward the surface. The MITgcm outputs suggested that the northward gradient of heat loss tilts the isopycnals, which gradually deepen toward the north, thereby enabling baroclinic instabilities and hence the eddy generation (Zhan et al. 2016). The EKE dominates the mean-flow kinetic energy (Zhan et al. 2016), with the fate of observed eddies being largely governed by atmospheric forcing and local ocean conditions (Zhan et al. 2018). Driven by considerable heat fluxes, intensified eddy activity promotes convection processes, especially during winter in the north (Papadopoulos et al. 2013, 2015). The northward transport of warmer and fresher water by eddies reduces the intrinsic meridional gradient and flattens the isopycnals, which in turn limits the eddy generation and was interpreted as a typical negative feedback mechanism

(Zhan et al. 2019). Based on WRF–MITgcm–CMS simulations, the Red Sea mesoscale circulation was found to play an important role in transporting biogeochemical tracers within the basin (Fig. 9) and in supporting the marine ecosystem (Zhan et al. 2014; Dreano et al. 2016; Raitsos et al. 2017; Guo et al. 2021, manuscript submitted to *J. Geophys. Res. Oceans*).

Tides. The main tidal signal in the Red Sea propagates from the Arabian Sea through BaM. Observations and simulations suggest a high variability of tidal elevation with latitude, with the northern and southern basins exhibiting relatively large amplitudes compared to the central basin (Guo et al. 2016). Barotropic tides generate internal tides and solitary waves, mainly on the steep sides of the deep trough in the southern part of the Red Sea (da Silva et al. 2012; Guo et al. 2016). Our simulations using a 200-m nonhydrostatic MITgcm and CMS showed that the breaking of internal waves induces vertical mixing, which could increase the supply of nutrients to the euphotic zone and enhance biological productivity, by disrupting the pycnocline and inducing turbulence (Guo et al. 2020, manuscript submitted to *J. Geophys. Res. Oceans*).

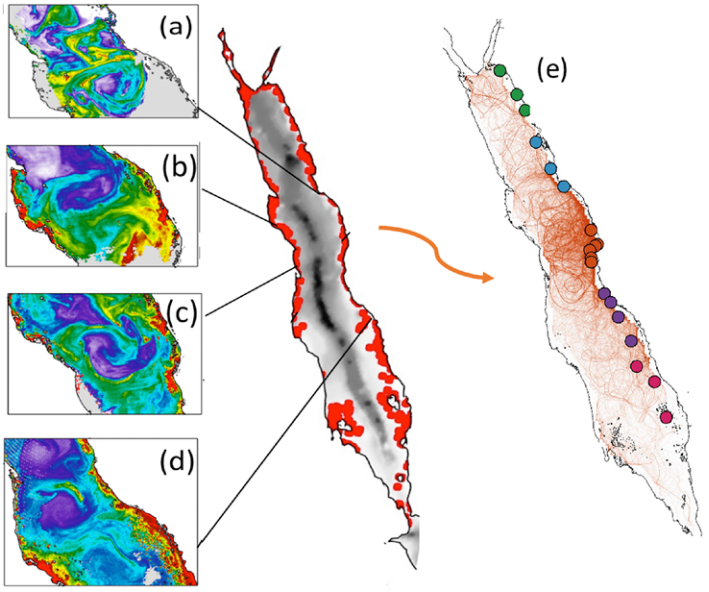

Fig. 9. Remotely sensed ocean color observations portraying surface flow (eddies and currents) between coral reefs in the Red Sea. (a)–(d) Chlorophyll (mg m^{-3}) patterns at different time periods (1 Jun 2010, 21 Jun 2009, 4 Mar 2006, and 13 Apr 2001, respectively) illustrating the impact of the basinwide mesoscale variability on the basin productivity. The central map depicts seafloor elevation and the position of coral reefs (red circles) in the Red Sea (coral reef positions were acquired from Global Distribution of Coral Reefs 2010; https://data.unep-wcmc.org/datasets/1). (e) Simulated particle dispersion trajectories forming pathways of connectivity in the Red Sea. Particles were released from the locations of the coral reefs along the east coast of the central Red Sea. The different colors denote each of the five different Red Sea provinces (Raitsos et al. 2013). The panel suggests basinwide connectivity with the central Red Sea driven by mesoscale activity, except for the southern Red Sea, which connects more with the Gulf of Aden (Raitsos et al. 2017; Wang et al. 2019).

Waves. Based on long-term WWIII simulations forced with the in-house WRF downscaled Red Sea reanalysis, the wave variability in the Red Sea was naturally associated with the dominant regional wind regimes (Langodan et al. 2014). Although wind intensity in the basin is usually moderate, a prolonged duration and the existence of a long fetch may give rise to waves that reach up to 3.5 m. The irregular shape of the Red Sea coast creates shadowed areas, especially in the south where southward-moving waves reduce to swell and propagate unidirectionally. During summer, consistent northwesterly winds generate mean wave heights of 1–1.5 m in the north, frequently exceeding 2 m (Langodan et al. 2014, 2018). The southward wave system persists throughout the year, while the northward system associated with the monsoon winds exhibits a well-defined seasonality between October and April (Langodan et al. 2018). The coexistence of northward and southward waves in winter creates a convergence zone in the central Red Sea (Langodan et al. 2015). Various transversal jets, such as the Tokar jet on the Sudan coast and others that originate in the AP generate locally dominant wave regimes (Langodan et al. 2017b). These exhibit strong seasonality and are usually dominated by other systems.

Ecological indicators. The recent development of multisensor satellite missions, such as the Ocean Color Climate Change Initiative (OC-CCI; Sathyendranath et al. 2019), has increased

the coverage of surface Chl-a measurements in the Red Sea by enhancing the retrieval of satellite data under adverse atmospheric conditions. Using available in-water measurements of Chl-a, Brewin et al. (2013, 2019) and Racault et al. (2015) have shown that both standard ocean-color algorithms and the OC-CCI algorithm perform well in the Red Sea, but further improvements have been achieved by developing a regional algorithm specifically tuned to the basin (Brewin et al. 2015).

The analysis of the derived long-term Chl-a dataset together with the MITgcm, WRF, CMS, and ERSEM simulations has enabled an unprecedented understanding of the general functioning of the Red Sea ecosystem and its productivity. The open waters of the Red Sea Chl-a exhibit a distinct seasonality with maximum concentrations seen during wintertime, which was attributed to vertical mixing in the north and wind-induced horizontal intrusion of nutrient-rich water in the south, and minimum concentrations during summer (Raitsos et al. 2013). However, large sporadic blooms have been reported during summer in the coastal southern Red Sea driven by the GAIW (Racault et al. 2015; Dreano et al. 2016). The concentration and the duration of the phytoplankton growing season in the Red Sea are modulated by the strength of the winter monsoon over the Arabian Sea, which affects the horizontal advection of fertile waters from the Indian Ocean (Raitsos et al. 2015). Warmer conditions over the region were also associated with substantially weaker winter phytoplankton blooms, which initiate later and are shorter in their overall duration (~4 weeks) (Gittings et al. 2018, 2019). Satellite-derived estimates of phytoplankton size structure are in good agreement with the in situ measurements, and also capture the spatial variability related to regional mesoscale dynamics (Gittings et al. 2019b). iReds outputs were also used along with in situ and satellite observations to investigate the basin ecological responses to the combined effects of biogeochemical and physical environmental stressors (Ellis et al. 2019).

High-resolution nested modeling in support of new mega-developments along the Red Sea coast.

Met-ocean modeling in NEOM. NEOM spreads over an area of 26,500 km^2 along the northern Red Sea coast of Saudi Arabia, bordering Jordan and Egypt. To support environmental impact assessment efforts and to generate essential met-ocean data required for initial planning, high-resolution atmospheric and oceanic models were implemented and nested within the regional Red Sea models. A 3-yr 600-m-resolution WRF simulation was performed to investigate the orographic influence on the coastal atmospheric conditions and to drive high-resolution coastal ocean models. Air quality was also investigated using HYSPLIT driven by the WRF fields to study dispersion of pollutants and their diurnal variations in relation to the land–sea breezes and boundary layer heights (Dasari et al. 2020).

The large-scale ocean circulation of the NEOM region simulated by the regional MITgcm suggests numerous eddy features, with the topography being the critical factor driving their interactions. A coupled Delft3D + SWAN model configuration with horizontal resolution of 50 m and 10 vertical sigma levels was nested within MITgcm to resolve the coastal circulations and was forced with tides and 600-m WRF fields. Seasonal simulations highlighted different coastal circulation features, including a prominent localized eddy-like structure in the center of the NEOM lagoon where the inner water connects with the open ocean through a narrow channel, and a persistent northwest–southeast current along the broad offshore edge of the coral reefs. The "residence time" estimates based on trajectories of simulated passive particles suggests a faster ventilation rate in winter. The SWAN model nested within the regional WWIII suggested a dominance of locally generated waves in the southeast direction, with a maximum significant wave height of ~0.8 m, associated with consistent strong northwesterlies.

Extreme waves and water levels for KAEC. KAEC is a new city under development along the western Saudi coast, comprising the largest port on the Red Sea, residential districts, and an industrial valley. The area is surrounded by coral reefs and includes a shallow lagoon on its southern side. We supported the development of the sea wall for coastal protection by providing estimates of extreme wave heights and water levels for the KAEC shoreline. For this, we used a coupled ADCIRC + SWAN model configured on a triangular grid with an open boundary in the Arabian Sea. The model's unstructured-grid resolution varied from a maximum vertex spacing of approximately 60 km near the boundary down to 60 m near the KAEC coastline. The bathymetry was generated from 0.5-m-resolution lidar surveys of the KAEC coast. Simulations were carried out for a 30-yr period, forced with the our WRF downscaled atmospheric reanalysis. Extreme value analyses were applied to estimate different return levels of wave heights and water levels. The model effectively simulated the dampening of the offshore waves propagating toward the shoreline by the coral reefs (Fig. 10). The KAEC coastline being characterized by a weak tidal regime, extreme sea levels are dominated by meteorological activity, mostly observed during winter. The 100-yr return levels of wave heights and water level were estimated at 70 and 65 cm, respectively, only marginally (~5 cm) different from the 30-yr maxima (Langodan et al. 2020b; Antony et al. 2021).

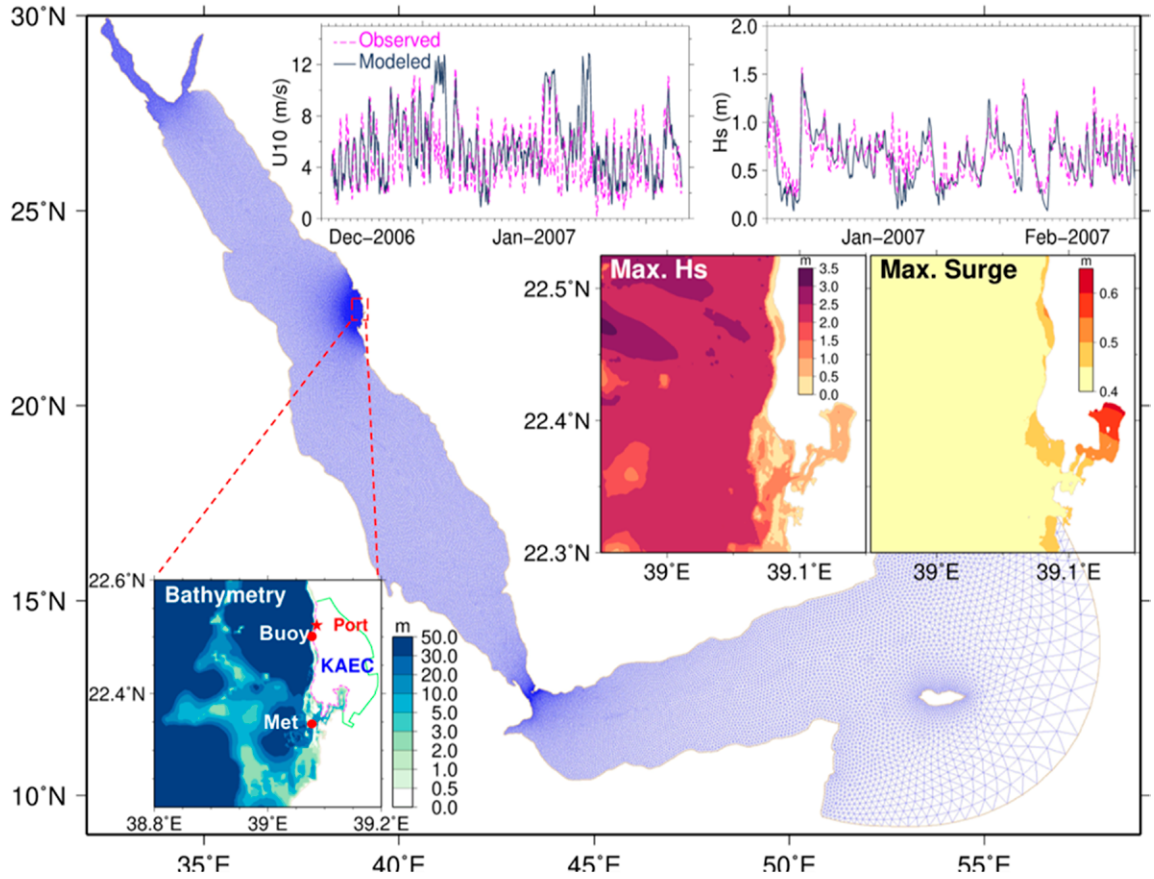

Fig. 10. Coupled ADCIRC + SWAN model domain used for estimating extreme wave heights and water levels along the KAEC coastline. The unstructured grid resolution varies from 60 km near the boundary in the Arabian Sea to 60 m near the KAEC coastline. The bathymetry of the KAEC and maximum of significant wave heights and water levels from 30-yr simulations are also shown in the inset images. The model–data comparisons at the locations indicated in the bathymetry plot ("Met" for winds and "Buoy" for waves) suggest a good agreement between the model simulations and the measurements.

Regional forecasting applications

Extreme rainfall forecasting. The KSA is characterized by a hot and arid desert climate. Occasionally, extreme precipitation events over the Jeddah region have led to flooding that caused extensive loss of human life and damage to infrastructure (e.g., de Vries et al. 2013). The large-scale features are important factors in producing regional extreme precipitation, which may exceed 3 times the average annual rainfall. These heavy rainfall events are associated with the northward extension of the Red Sea trough and intensification of the Arabian anticyclone, which provide warm moist air to the region, creating favorable conditions for the development of a short-lived quasi-stationary mesoscale convective systems (Dasari et al. 2018). Using a convective-permitting WRF configuration, Viswanadhapalli et al. (2016) assessed the predictability of two extreme rainfall events formed over Jeddah while assimilating various combinations of conventional and satellite observations (Fig. 11a). A similar WRF configuration was implemented by Dasari et al. (2017) to study the Mecca 2016 extreme rainfall event. More recently, Luong et al. (2020) investigated the impact of urbanization using WRF by incorporating an urban canopy model and urban land cover for several extreme weather events over Jeddah showing that urbanization enhanced rainfall by ~25%.

Oil spill forecasting. iReds is regularly used to support oil spill prediction efforts. As an example, we have supported the Saudi authorities in the southern Red Sea by simulating a realistic oil spill scenario from an abandoned oil tanker filled with oil and anchored at Ras Isa port north of Hudaydah off the coast of Yemen. The ship, which has not been operational since March 2015, is corroding and there are serious concerns that the gas building up in the storage tanks could lead to an explosion that might trigger an oil spill (Meredith 2019). The tanker carries an estimated volume of 1 million barrels of crude oil, 4 times the amount of oil released in the 1989 Exxon Valdez oil spill. MEDSLIK was used to model the transport and fate of oil for winter and summer scenarios. Forecast winds, waves and ocean currents generated by iReds during the first 2 weeks of February and August 2019 have been used as

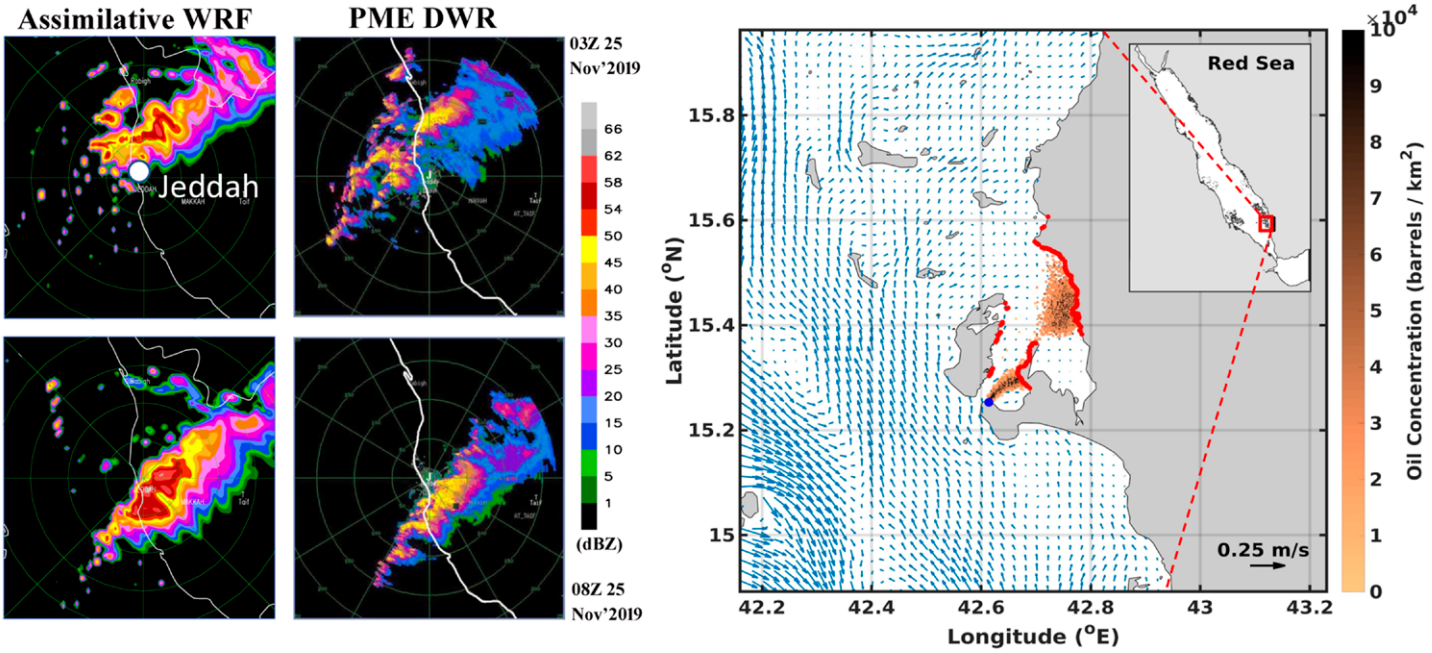

Fig. 11. (a) Evolution of reflectivity as predicted by WRF with assimilation of conventional and satellite radiance data against PME DWR data during Jeddah extreme rainfall event at 0300 and 0800 UTC 25 Nov 2009 (Viswanadhapalli et al. 2016). (b) Concentration of oil (in barrels km^2) after 14 days of spill from the tanker location marked by the blue dot. Red dots indicate beached spill locations. The investigated region is indicated by the red box in the inset Red Sea basin panel.

inputs. The oil was continuously released at the tanker location (15°15′11″N, 42°36′52″E) over the 2-week simulation period. Figure 11b shows the concentration of oil (in barrels km^{-2}) at the end of the simulation period. Following the pattern of the predicted ocean circulation, the oil was transported northeast, where about 60% of its volume washed up onshore. Twenty percent of the remaining oil formed a surface slick of about 55 km^2 in size and the other 20% evaporated.

Future directions

iReds has so far contributed new insights into the regional atmospheric and oceanic circulations, their variability, and trends in the Red Sea basin. Outputs from its various long-term simulations established, in particular, a unique basinwide eddy activity and its driving forces, a prominent seasonally varying overturning circulation modulated by the Indian monsoon, and the occasional fast ventilation of its deep waters through deep water formation events forced by cold weather anomalies in its northern end. The system was further critically important in supporting the ongoing mega-projects along the Red Sea shores, providing unique information about the regional environment to optimize the design and the operations of these new developments. It further developed for the first time regionally tuned forecasting capabilities that were successfully tested during urgent environmental situations.

We are envisioning, and have already started working along several directions, to implement new capabilities and continue enhancing iReds performances in the future, while further deepening our understanding of the regional circulation and variability. Our ultimate goal is to develop an integrated data-driven modeling and forecasting system that incorporates all available oceanic and atmospheric observations in the Red Sea region and makes predictions and actionable information available to scientists, government and industry, and nonexpert recipients. In this regard, the first Red Sea operational system is expected to be released online during 2021 to provide weekly forecasts of the basinwide atmospheric (WRF)–oceanic (MITgcm)–wave (WWIII) conditions at 4-, 2-, and 1-km resolutions, respectively. It will be subsequently equipped with state-of-the-art interactive visualization and data analytics to provide decision makers with real-time access to relevant information. Future work will then focus on (i) equipping iReds with new capabilities for forecasting aerosols (dust and pollution) and the marine biogeochemistry and (ii) extending the forecasting time range of the system to subseasonal-to-seasonal and annual scales through a combination of coupled modeling and data assimilation, and spatial range to the urban and coastal scales through downscaling.

iReds developments. Beyond the importance of predicting dust and atmospheric pollution, aerosols play a crucial role in the radiation budget and the development of clouds and precipitation. They are also an important source of nutrients for the Red Sea ecosystem. So far, aerosol variations have only been climatologically accounted for in iReds. WRF is equipped with state-of-the-art modules to simulate and study aerosols (WRF-Chem), and we have recently implemented it over the AP. We are currently working on developing high-resolution aerosol emission inventories (natural, anthropogenic, and biogenic) on daily scales by tuning satellite remote sensing retrieval algorithms with available in situ measurements. These will be incorporated/assimilated into WRF-Chem to simulate and predict dust storms and outbreaks of industrial and urban haze pollution.

As part of the newly established Center of Excellence for NEOM research at KAUST, our modeling system will be further expanded to investigate oceanic and atmospheric circulations at the urban scales. Work is already underway with external collaborators at Imperial College (United Kingdom) and Deltares Institute (Netherlands) to build the required computational fluid dynamics (CFD) algorithms in order to downscale our models' outputs and capabilities at these scales. In this regard, we have further recently introduced and successfully tested a

new dynamical downscaling algorithm with WRF, based on the continuous data assimilation approach (Desamsetti et al. 2019). Downscaling ensembles from the global operational centers remain computationally demanding in terms of both computational cost and storage. We will investigate novel approaches for identifying efficient downscaling of probabilistic maps through machine and dynamical learning approaches.

In terms of data assimilation, we will continue working on enhancing the skills of our ensemble system. In particular, proper accounting of model errors, for instance, through stochastic perturbations and forcing ensembles greatly enhanced the assimilation results. Developing data-driven approaches for quantifying the uncertainties of such perturbations and eventually estimating their parameters as part of the assimilation process is our next target. To extend the time range of the system predictability, we will also strongly couple the WRF–DART and MITgcm–DART ensemble assimilation systems to simultaneously exploit the observations of both components.

General circulation and climate of the Red Sea and their impact on the ecosystem

While the upper general circulation of the Red Sea is now relatively well understood, little is still known about the deep circulation. Based on chemical tracers, it has been suggested that a deep overturning cell is present, but our ongoing investigations suggest a more complex 3D circulation with the existence of a basinwide cyclonic gyre in addition to the deep overturning circulation. Insight into the variability and ventilation of the RSDW is needed to advance our understanding of the general circulation of the Red Sea. We are further implementing nonhydrostatic configurations of the MITgcm with variable-resolution curvilinear grids zooming (~100 m) on the straits to resolve in more detail the features of the water exchange with the Indian Ocean through BaM and the water formation and sinking in the north.

Monitoring the decadal and seasonal variability of Red Sea ecosystem indicators, in relation to the regional environmental conditions and broader climate change, is a necessity for the sustainability of marine life and responsible stewardship of its socio-economical assets. Toward this end, we have synergistically combined remotely sensed ocean-color observations with our models' simulations to investigate various aspects of the Red Sea ecosystem in this historically data-sparse region. Remote sensing will continue to be an integral component of our system, providing information for model validation and assimilation, and predicting how the ecosystem indicators would respond to a changing climate. Currently, we are also developing regionally tuned algorithms for high-resolution satellite sensors (<300-m resolution) that would be particularly useful for tackling ecological issues in the coastal economic zone of the Red Sea. In parallel, we will generate interannual simulations with the ecosystem model, which has been only investigated so far with climatological physical forcing. This multidisciplinary approach is expected to offer new insights into the past and current environmental status of the Red Sea coastal zone and to help us to identify vulnerable regions as well as biodiversity hotspots.

Coupled processes, predictability, and forecasting at seasonal and climate scales

The capabilities of the newly developed SKRIPS coupled model are yet to be fully exploited. We will intensify studies using this system to understand coupled phenomena in the Red Sea region at short- and long-term scales, and how those respond to the global climate dynamics and variations. We are currently examining the outputs of the ocean-waves coupling component to investigate wave–current interactions and coastal circulations, with particular interest in the water exchanges near and over the coral reefs. Another proposed development of SKRIPS is the coupling of the atmospheric chemical and marine ecosystem components to investigate regional carbon variations and exchanges.

This coupled system will be at the core of building long-term regional predictive capabilities at the subseasonal-to-seasonal through climate scales by downscaling global forecasts and

climate change scenarios. We will assess the system predictability of the regional phenomenon at different scales, including extreme weather events (heavy rainfall, air and marine heatwaves). The focus will be on identifying key factors and dynamical processes that may provide extended predictability for the region and on quantifying their impact on the forecasting skills through sensitivity studies. These will be then used as a guide for designing efficient, regionally tuned, data-driven strategies for projecting the weather and climate of the Red Sea and their impact on the regional ecosystem and Red Sea coast.

Acknowledgments. Dedicated to the bright memory of Professor Trevor Platt, a pioneer in biological oceanography and a key contributor to Red Sea research. The development of the Red Sea modeling system is being supported by the Virtual Red Sea Initiative and the Competitive Research Grants (CRG) program from the Office of Sponsored Research at KAUST, Saudi Aramco Company through the Saudi ARAMCO Marine Environmental Center at KAUST, and by funds from KAEC, NEOM, and RSP through Beacon Development Company at KAUST.

Appendix: List of Acronyms and Abbreviations

Table A1 contains a list of acronyms and abbreviations used in the paper.

Table A1. Acronyms and abbreviations.

Acronym/abbreviation	Expansion
3DVAR	Three-dimensional variational data assimilation
4DVAR	Four-dimensional variational data assimilation
ADCIRC	Advanced circulation
AMSU	Advanced Microwave Sounding Unit
AOD	Aerosol optical depth
AP	Arabian Peninsula
APHRODITE	Asian Precipitation–Highly Resolved Observational Data Integration Towards Evaluation
ASCAT	Advanced Scatterometer
AVHRR	Advanced Very High Resolution Radiometer
AWS	Automatic weather station
BaM	Bab-al-Mandeb
CCMP	Cross-calibrated multi-platform
AMSU	Advanced Microwave Sounding Unit
ASCAT	Advanced Scatterometer
AVISO	Archiving, Validation, and Interpretation of Satellite Oceanographic Data
Chl-a	Chlorophyll-a
CFD	Computational fluid dynamics
CMEMS-L4	Copernicus Marine Environment Monitoring Service
CMORPH	Climate Prediction Center morphing technique
CMS	Connectivity modeling system
CRU	Climatic Research Unit
DART	Data Assimilation Research Testbed
DWR	Doppler weather radar
EAKF	Ensemble adjustment Kalman filter
ECCO	Estimating the Circulation and Climate of the Ocean
ECCO2	Estimating the Circulation and Climate of the Ocean, Phase II
ECMWF	European Centre for Medium-Range Weather Forecasts
EKE	Eddy kinetic energy
ERA	ECMWF Re-Analysis

Table A1. (*Continued*).

Acronym/abbreviation	Expansion
ERSEM	European Regional Seas Ecosystem Model
ESA	European Space Agency
ESMF	Earth System Modeling Framework
FNL	Final analysis
GAIW	Gulf of Aden Intrusion Water
GDP	Gross domestic product
GHRSST	Group for High Resolution Sea Surface Temperature
GLORYS2	Global Ocean Reanalysis 2
GPSRO	Global Position System Radio Occultation
HYCOM	Hybrid Coordinate Ocean Model
HYSPLIT	Hybrid Single-Particle Lagrangian Integrated Trajectory
iReds-M1	Integrated data-driven Red Sea Modeling system version 1
KAEC	King Abdullah Economic City
KAUST	King Abdullah University of Science and Technology
KSA	Kingdom of Saudi Arabia
LME	Large marine ecosystem
MITgcm	Massachusetts Institute of Technology general circulation model
NCEP	National Centers for Environmental Prediction
NUOPC	National United Operational Prediction Capability
OC-CCI	Ocean Color Climate Change Initiative
OLCI	Ocean and Land Color Instrument
OSTIA	Operational Sea Surface Temperature and Sea Ice Analysis
OTIS	The Ohio State University Tidal Inversion Software
PME	Presidency of Meteorology and Environment
RADS	Radar Altimeter Database
RMSE	Root-mean-square error
RSDW	Red Sea Deep Water
RSOW	Red Sea Outflow Water
RSP	Red Sea Project
SKRIPS	Scripps–KAUST Regional Integrated Prediction System
SSH	Sea surface height
SST	Sea surface temperature
SWAN	Simulating Waves Nearshore
TRMM	Tropical Rainfall Measuring Mission
WHOI	Woods Hole Oceanographic Institution
WOA	World Ocean Atlas
WRF	Weather Research and Forecasting
WWIII	WaveWatch-III

References

Afzal, S., M. Hittawe, S. Ghani, T. Jamil, O. Knio, M. Hadwiger, and I. Hoteit, 2019a: The state of the art in visual analysis approaches for ocean and atmospheric datasets. *Comput. Graphics Forum*, **38**, 881–907, https://doi.org/10.1111/cgf.13731.

——, and Coauthors, 2019b: RedSeaAtlas: A visual analytics tool for spatio-temporal multivariate data of the Red Sea. *Workshop on Visualization in Environmental Sciences (EnvirVis)*, Porto, Portugal, Eurographics Association, 25–32, https://doi.org/10.2312/envirvis.20191101.

Albarakati, S., R. M. Lima, L. Giraldi, I. Hoteit, and O. Knio, 2019: Optimal 3D trajectory planning for AUVs using ocean general circulation models. *Ocean Eng.*, **188**, 106266, https://doi.org/10.1016/j.oceaneng.2019.106266.

Anderson, J., T. Hoar, K. Raeder, H. Liu, N. Collins, R. Torn, and A. Avellano, 2009: The Data Assimilation Research Testbed: A community facility. *Bull. Amer. Meteor. Soc.*, **90**, 1283–1296, https://doi.org/10.1175/2009BAMS2618.1.

Antony, C., S. Langodan, P. R. Shanas, H. P. Dasari, Y. Abualnaja, O. Knio, and I. Hoteit, 2021: Extreme water levels along the central Red Sea coast of Saudi Arabia: processes and frequency analysis. *Nat. Hazards*, https://doi.org/10.1007/s11069-020-04377-y, in press.

Ardhuin, F., and Coauthors, 2010: Semiempirical dissipation source functions for ocean waves. Part I: Definition, calibration and validation. *J. Phys. Oceanogr.*, **40**, 1917–1941, https://doi.org/10.1175/2010JPO4324.1.

Attada, R., H. P. Dasari, J. S. Chowdary, Y. Ramesh Kumar, O. Knio, and I. Hoteit, 2018a: Surface air temperature variability over the Arabian Peninsula and its links to circulation patterns. *Int. J. Climatol.*, **39**, 445–464, https://doi.org/10.1002/joc.5821.

——, R. K. Yadav, R. K. Kunchala, H. P. Dasari, O. Knio, and I. Hoteit, 2018b: Prominent modes of summer surface air temperature variability and associated circulation anomalies over the Arabian Peninsula. *Atmos. Sci. Lett.*, **19**, e860, https://doi.org/10.1002/asl.860.

——, H. P. Dasari, A. Parekh, J. S. Chowdary, S. Langodan, O. Knio, and I. Hoteit, 2018c: The role of the Indian summer monsoon variability on Arabian Peninsula summer climate. *Climate Dyn.*, **52**, 3389–3404, https://doi.org/10.1007/s00382-018-4333-x.

Baretta, J. W., W. Ebenhoh, and P. Ruardij, 1995: The European-Regional-Seas-Ecosystem-Model, a complex marine ecosystem model. *Neth. J. Sea Res.*, **33**, 233–246, https://doi.org/10.1016/0077-7579(95)90047-0.

Barker, D., and Coauthors, 2012: The Weather Research and Forecasting Model's Community Variational/Ensemble Data Assimilation System: WRFDA. *Bull. Amer. Meteor. Soc.*, **93**, 831–843, https://doi.org/10.1175/BAMS-D-11-00167.1.

Belkin, I. M., 2009: Rapid warming of large marine ecosystems. *Prog. Oceanogr.*, **81**, 207–213, https://doi.org/10.1016/j.pocean.2009.04.011.

Booij, N., R. C. Ris, and L. H. Holthuijsen, 1999: A third-generation wave model for coastal regions. Part 1: Model description and validation. *J. Geophys. Res.*, **104**, 7649–7666, https://doi.org/10.1029/98JC02622.

Brewin, R. J. W., D. E. Raitsos, Y. Pradhan, and I. Hoteit, 2013: Comparison of chlorophyll in the Red Sea derived from MODIS-Aqua and in vivo fluorescence. *Remote Sens. Environ.*, **136**, 218–224, https://doi.org/10.1016/j.rse.2013.04.018.

——, and Coauthors, 2015: Regional ocean-colour chlorophyll algorithms for the Red Sea. *Remote Sens. Environ.*, **165**, 64–85, https://doi.org/10.1016/j.rse.2015.04.024.

——, and Coauthors, 2019: Factors regulating the relationship between total and size-fractionated chlorophyll-a in coastal waters of the Red Sea. *Front. Microbiol.*, **10**, 1964, https://doi.org/10.3389/fmicb.2019.01964.

Cantin, N. E., A. L. Cohen, K. B. Karnauskas, A. M. Tarrant, and D. C. McCorkle, 2010: Ocean warming slows coral growth in the central Red Sea. *Science*, **329**, 322–325, https://doi.org/10.1126/science.1190182.

Carvalho, S., B. Kürten, G. Krokos, I. Hoteit, and J. Ellis, 2018: The Red Sea. *World Seas: An Environmental Evaluation*, Vol. II, *The Indian Ocean to the Pacific*, Academic Press, 49–74.

Cember, R. P., 1988: On the sources, formation, and circulation of Red Sea deep water. *J. Geophys. Res.*, **93**, 8175–8191, https://doi.org/10.1029/JC093iC07p08175.

Chaidez, V., D. Dreano, S. Agusti, C. M. Duarte, and I. Hoteit, 2017: Decadal trends in Red Sea maximum surface temperature. *Sci. Rep.*, **7**, 8144, https://doi.org/10.1038/s41598-017-08146-z.

Churchill, J. H., Y. Abualnaja, R. Limeburner, and M. Nellayaputhenpeedika, 2018: The dynamics of weather-band sea level variations in the Red Sea. *Reg. Stud. Mar. Sci.*, **24**, 336–342, https://doi.org/10.1016/j.rsma.2018.09.006.

Collingridge, K., 2012: Modelling risk areas in the North Sea for blooms of the invasive comb jellyfish *Mnemiopsis leidyi* A. Agassiz, 1865. *Aquatic Invasions*, **9**, 21–36, https://doi.org/10.3391/ai.2014.9.1.02.

Dasari, H. P., A. Raju, O. Knio, and I. Hoteit, 2017: Analysis of a severe weather event over Mecca, Kingdom of Saudi Arabia using observations and high-resolution modeling. *Meteor. Appl.*, **24**, 612–627, https://doi.org/10.1002/met.1662.

——, L. Sabique, V. Yesubabu, V. B. Rao, V. P. Papadopoulos, and I. Hoteit, 2018: ENSO influence on the Red Sea convergence zone and associated rainfall. *Int. J. Climatol.*, **38**, 761–775, https://doi.org/10.1002/joc.5208.

——, S. Desamsetti, S. Langodan, R. Attada, R. K. Kunchala, Y. Viswanadhapalli, O. Knio, and I. Hoteit, 2019: High-resolution assessment of solar energy resources over the Arabian Peninsula. *Appl. Energy*, **248**, 354–371, https://doi.org/10.1016/j.apenergy.2019.04.105.

——, ——, ——, S. Singh, L. N. K. Ramakrishna, and I. Hoteit, 2020: Air-quality assessment over NEOM, Kingdom of Saudi Arabia. *Atmos. Environ.*, **230**, 117489, https://doi.org/10.1016/j.atmosenv.2020.117489.

da Silva, J., J. Magalhaes, T. Gerkema, and L. Maas, 2012: Internal solitary waves in the Red Sea: An unfolding mystery. *Oceanography*, **25**, 96–107, https://doi.org/10.5670/oceanog.2012.45.

Davis, S. R., L. J. Pratt, and H. Jiang, 2015: The Tokar Gap: Regional circulation, diurnal variability, and moisture transport based on numerical simulations. *J. Climate*, **28**, 5885–5907, https://doi.org/10.1175/JCLI-D-14-00635.1.

De Dominicis, M., N. Pinardi, G. Zodiatis, and R. Archetti, 2013a: MEDSLIK-II, a Lagrangian marine surface oil spill model for short-term forecasting - Part II: Numerical simulations and validations. *Geosci. Model Dev.*, **6**, 1871–1888, https://doi.org/10.5194/gmd-6-1871-2013.

——, ——, ——, and R. Lardner, 2013b: MEDSLIK-II, a Lagrangian marine surface oil spill model for short-term forecasting - Part I: Theory. *Geosci. Model Dev.*, **6**, 1851–1869, https://doi.org/10.5194/gmd-6-1851-2013.

Deltares, 2016: Delft3D-FLOW: Simulation of multi-dimensional hydrodynamic flow and transport phenomena, including sediments. User manual, version 3.15, Deltares, 684 pp., https://oss.deltares.nl/documents/183920/185723/Delft3D-FLOW_User_Manual.pdf.

Desamsetti, S., H. P. Dasari, S. Langodan, E. S. Titi, O. Knio, and I. Hoteit, 2019: Efficient dynamical downscaling of general circulation models using continuous data assimilation. *Quart. J. Roy. Meteor. Soc.*, **145**, 3175–3194, https://doi.org/10.1002/qj.3612.

de Vries, A. J., E. Tyrlis, D. Edry, S. O. Krichak, B. Steil, and J. Lelieveld, 2013: Extreme precipitation events in the Middle East: Dynamics of the active Red Sea trough. *J. Geophys. Res. Atmos.*, **118**, 7087–7108, https://doi.org/10.1002/jgrd.50569.

Draxler, R. R., and G. D. Hess, 1997: Description of the HYSPLIT_4 modeling system. NOAA Tech. Memo. ERL ARL-224, NOAA/Air Resources Laboratory, Silver Spring, MD, 24 pp., www.arl.noaa.gov/documents/reports/arl-224.pdf.

Dreano, D., D. E. Raitsos, J. Gittings, G. Krokos, and I. Hoteit, 2016: The Gulf of Aden intermediate water intrusion regulates the Southern Red Sea summer phytoplankton blooms. *PLOS ONE*, **11**, e0168440, https://doi.org/10.1371/journal.pone.0168440.

Edwards, A., and S. Head, Eds., 1987: *Red Sea*. Key Environment Series, Pergamon Press, 451 pp.

Edwards, C., A. Moore, I. Hoteit, and B. Cornuelle, 2015: Regional ocean data assimilation. *Annu. Rev. Mar. Sci.*, **7**, 21–42, https://doi.org/10.1146/annurev-marine-010814-015821.

Ellis, J. I., and Coauthors, 2019: Multiple stressor effects on coral reef ecosystems. *Global Change Biol.*, **25**, 4131–4146, https://doi.org/10.1111/gcb.14819.

El Mohtar, S., I. Hoteit, O. Knio, L. Issa, and I. Lakkis, 2018: Lagrangian tracking in stochastic fields with application to an ensemble of velocity fields in the Red Sea. *Ocean Modell.*, **131**, 1–14, https://doi.org/10.1016/j.ocemod.2018.08.008.

Eshel, G., M. A. Cane, and M. B. Blumenthal, 1994: Modes of subsurface, intermediate, and deep water renewal in the Red Sea. *J. Geophys. Res.*, **99**, 15 941–15 952, https://doi.org/10.1029/94JC01131.

Genevier, L. G. C., T. Jamil, D. E. Raitsos, G. Krokos, and I. Hoteit, 2019: Marine heatwaves reveal coral reef zones susceptible to bleaching in the Red Sea. *Global Change Biol.*, **25**, 2338–2351, https://doi.org/10.1111/gcb.14652.

Gimeno, L., A. Drumond, R. Nieto, R. M. Trigo, and A. Stohl, 2010: On the origin of continental precipitation. *Geophys. Res. Lett.*, **37**, L13804, https://doi.org/10.1029/2010GL043712.

Gittings, J. A., D. E. Raitsos, G. Krokos, and I. Hoteit, 2018: Impacts of warming on phytoplankton abundance and phenology in a typical tropical marine ecosystem. *Sci. Rep.*, **8**, 2240, https://doi.org/10.1038/s41598-018-20560-5.

——, R. J. W. Brewin, D. E. Raitsos, M. Kheireddine, M. Ouhssain, B. H. Johns, and I. Hoteit, 2019a: Remotely sensing phytoplankton size structure in the Red Sea. *Remote Sens. Environ.*, **234**, 111387, https://doi.org/10.1016/j.rse.2019.111387.

——, D. E. Raitsos, M. Kheireddine, M. F. Racault, H. Claustre, and I. Hoteit, 2019b: Evaluating tropical phytoplankton phenology metrics using contemporary tools. *Sci. Rep.*, **9**, 674, https://doi.org/10.1038/s41598-018-37370-4.

Guo, D., T. R. Akylas, P. Zhan, A. Kartadikaria, and I. Hoteit, 2016: On the generation and evolution of internal solitary waves in the southern Red Sea. *J. Geophys. Res. Oceans*, **121**, 8566–8584, https://doi.org/10.1002/2016JC012221.

——, A. Kartadikaria, P. Zhan, J. S. Xie, M. J. Li, and I. Hoteit, 2018: Baroclinic tides simulation in the Red Sea: Comparison to observations and basic characteristics. *J. Geophys. Res. Oceans*, **123**, 9389–9404, https://doi.org/10.1029/2018JC013970.

Hadri, B., S. Kortas, S. Feki, R. Khurram, and G. Newby, 2015: Overview of the KAUST's Cray X40 system–Shaheen II. *Proc. 2015 Cray User Group*, Chicago, IL, Cray User Group, 7 pp., https://cug.org/proceedings/cug2015_proceedings/includes/files/pap129.pdf.

Hill, C., C. DeLuca, M. Balaji, M. Suarez, and A. Da Silva, 2004: The architecture of the Earth system modeling framework. *Comput. Sci. Eng.*, **6**, 18–28, https://doi.org/10.1109/MCISE.2004.1255817.

Höllt, T., A. Magdy, G. Chen, G. Gopalakrishnan, I. Hoteit, C. D. Hansen, and M. Hadwiger, 2013: Visual analysis of uncertainties in ocean forecasts for planning and operation of off-Shore structures. *IEEE Pacific Visualization Symp.*, Sydney, NSW, Australia, IEEE, 59–66, https://doi.org/10.1109/PacificVis.2013.6596144.

——, ——, P. Zhan, G. Chen, G. Gopalakrishnan, I. Hoteit, C. D. Hansen, and M. Hadwiger, 2014: Ovis: A framework for visual analysis of ocean forecast ensembles. *IEEE Trans. Visualization Comput. Graphics*, **20**, 1114–1126, https://doi.org/10.1109/TVCG.2014.2307892.

——, M. Hadwiger, O. Knio, and I. Hoteit, 2015: Probability maps for the visualization of assimilation ensemble flow data. *Workshop on Visualization in Environmental Sciences (EnvirVis)*, Cagliari, Italy, Eurographics Association, 43–47, https://doi.org/10.2312/envirvis.20151090.

Hoteit, I., B. Cornuelle, A. Köhl, and D. Stammer, 2006: Treating strong adjoint sensitivities in tropical eddy-permitting variational data assimilation. *Quart. J. Roy. Meteor. Soc.*, **131**, 3659–3682, https://doi.org/10.1256/qj.05.97.

——, T. Hoar, G. Gopalakrishnan, J. Anderson, N. Collins, B. Cornuelle, A. Kohl, and P. Heimbach, 2013: A MITgcm/DART ensemble analysis and prediction system with application to the Gulf of Mexico. *Dyn. Atmos. Oceans*, **63**, 1–23, https://doi.org/10.1016/j.dynatmoce.2013.03.002.

——, D. T. Pham, M. E. Gharamti, and X. Luo, 2015: Mitigating observation perturbation sampling errors in the stochastic EnKF. *Mon. Wea. Rev.*, **143**, 2918–2936, https://doi.org/10.1175/MWR-D-14-00088.1.

——, X. Luo, M. Bocquet, A. Kohl, and B. Ait-El-Fquih, 2018: Data assimilation in oceanography: Current status and new directions. *New Frontiers in Operational Oceanography*, E. P. Chassignet et al., Eds., GODAE Ocean View, 465–512, https://doi.org/10.17125/gov2018.

IOC, IHO, and BODC, 2003: Centenary edition of the GEBCO Digital Atlas. British Oceanographic Data Centre, CD-ROM.

Krokos, G., V. P. Papadopoulos, S. S. Sofianos, H. Ombao, P. Dybczak, and I. Hoteit, 2019: Natural climate oscillations may counteract Red Sea warming over the coming decades. *Geophys. Res. Lett.*, **46**, 3454–3461, https://doi.org/10.1029/2018GL081397.

Kunchala, R., R. Attada, H. P. Dasari, V. R. Kumar, S. Langodan, Y. Abualnaja, and I. Hoteit, 2018: Aerosol optical depth variability over the Arabian Peninsula as inferred from satellite measurement. *Atmos. Environ.*, **187**, 346–357, https://doi.org/10.1016/j.atmosenv.2018.06.011.

——, ——, ——, K. Ramesh, Y. Abualnaja, K. Ashok, and I. Hoteit, 2019: On the recent amplification of dust over the Arabian Peninsula during 2002-2012. *J. Geophys. Res. Atmos.*, **124**, 13220–13229, https://doi.org/10.1029/2019JD030695.

Langodan, S., L. Cavaleri, Y. Viswanadhapalli, and I. Hoteit, 2014: The Red Sea: A natural laboratory for wind and wave modeling. *J. Phys. Oceanogr.*, **44**, 3139–3159, https://doi.org/10.1175/JPO-D-13-0242.1.

——, ——, ——, and ——, 2015: Wind-wave source functions in opposing seas. *J. Geophys. Res. Oceans*, **120**, 6751–6768, https://doi.org/10.1002/2015JC010816.

——, Y. Viswanadhapalli, H. P. Dasari, O. Knio, and I. Hoteit, 2016a: A high resolution assessment of wind and wave energy potentials in the Red Sea. *Appl. Energy*, **181**, 244–255, https://doi.org/10.1016/j.apenergy.2016.08.076.

——, V. Yesubabu, and I. Hoteit, 2016b: The impact of atmospheric data assimilation on wave simulations in the Red Sea. *Ocean Eng.*, **116**, 200–215, https://doi.org/10.1016/j.oceaneng.2016.02.020.

——, L. Cavaleri, A. Pomaro, V. Yesubabu, L. Bertotti, and I. Hoteit, 2017a: The climatology of the Red Sea – Part 1: The winds. *Int. J. Climatol.*, **37**, 4518–4528, https://doi.org/10.1002/joc.5101.

——, ——, ——, ——, ——, and ——, 2017b: The climatology of the Red Sea – Part 2: The waves. *Int. J. Climatol.*, **37**, 4518–4528, https://doi.org/10.1002/joc.5101.

——, ——, ——, J. Portilla, Y. Abualnaja, and I. Hoteit, 2018: Unraveling climatic wind and wave trends in the Red Sea using wave spectra partitioning. *J. Climate*, **31**, 1881–1895, https://doi.org/10.1175/JCLI-D-17-0295.1.

——, ——, ——, ——, and ——, 2020a: Can we extrapolate climate in an inner basin? The case of the Red Sea. *Global Planet. Change*, **188**, 103151, https://doi.org/10.1016/j.gloplacha.2020.103151.

——, C. Antony, P. R. Shanas, H. P. Dasari, Y. Abualnaja, O. Knio, and I. Hoteit, 2020b: Wave modeling of a reef-sheltered coastal zone in the Red Sea. *Ocean Eng.*, **207**, 107378, https://doi.org/10.1016/j.oceaneng.2020.107378.

Luettich, R. A., and J. J. Westerink, 2004: Formulation and numerical implementation of the 2D/3D ADCIRC finite element model Version 44.XX. ADCIRC Tech. Rep., 74 pp., https://adcirc.org/files/2018/11/adcirc_theory_2004_12_08.pdf.

Luong, T. M., H. P. Dasari, and I. Hoteit, 2020: Impact of urbanization on the simulation of extreme rainfall in Jeddah, Saudi Arabia. *J. Appl. Meteor. Climatol.*, **59**, 953–971, https://doi.org/10.1175/JAMC-D-19-0257.1.

Marshall, J., A. Adcroft, C. Hill, L. Perelman, and C. Heisey, 1997a: A finite-volume, incompressible Navier Stokes model for studies of the ocean on parallel computers. *J. Geophys. Res.*, **102**, 5753–5766, https://doi.org/10.1029/96JC02775.

——, C. Hill, L. Perelman, and A. Adcroft, 1997b: Hydrostatic, quasi-hydrostatic, and nonhydrostatic ocean modeling. *J. Geophys. Res.*, **102**, 5733–5752, https://doi.org/10.1029/96JC02776.

Meredith, S., 2019: 'Floating bomb': Decaying oil tanker near Yemen coast could soon explode, experts warn. CNBC, 24 July, https://www.cnbc.com/2019/07/24/oil-tanker-near-yemen-coast-could-soon-explode-experts-warn.html.

Nanninga, G. B., P. Saenz-Agudelo, P. Zhan, I. Hoteit, and M. L. Berumen, 2015: Not finding Nemo: Limited reef-scale retention in a coral reef fish. *Coral Reefs*, **34**, 383–392, https://doi.org/10.1007/s00338-015-1266-2.

Osman, E. O., D. J. Smith, M. Ziegler, B. Kürten, C. Conrad, K. M. El-Haddad, C. R. Voolstra, and D. J. Suggett, 2018: Thermal refugia against coral bleaching throughout the northern Red Sea. *Global Change Biol.*, **24**, e474–e484, https://doi.org/10.1111/gcb.13895.

Papadopoulos, V. P., Y. Abualnaja, S. A. Josey, A. S. Bower, D. E. Raitsos, H. Kontoyiannis, and I. Hoteit, 2013: Atmospheric forcing of the winter air–sea heat fluxes over the northern Red Sea. *J. Climate*, **26**, 1685–1701, https://doi.org/10.1175/JCLI-D-12-00267.1.

——, and Coauthors, 2015: Factors governing the deep ventilation of the Red Sea. *J. Geophys. Res. Oceans*, **120**, 7493–7505, https://doi.org/10.1002/2015JC010996.

Paris, C. B., J. Helgers, E. van Sebille, and A. Srinivasan, 2013: Connectivity modeling system: A probabilistic modeling tool for the multi-scale tracking of biotic and abiotic variability in the Ocean. *Environ. Modell. Software*, **42**, 47–54, https://doi.org/10.1016/j.envsoft.2012.12.006.

Patzert, W. C., 1974: Wind induced reversal in the Red Sea circulation. *Deep-Sea Res.*, **21**, 109–121, https://doi.org/10.1016/0011-7471(74)90068-0.

Petihakis, G., G. Triantafyllou, I. J. Allen, I. Hoteit, and C. Dounas, 2002: Modelling the spatial and temporal variability of the Cretan Sea ecosystem. *J. Mar. Syst.*, **36**, 173–196, https://doi.org/10.1016/S0924-7963(02)00186-0.

Pratt, L. J., H. E. Deese, S. P. Murray, and W. Johns, 2000: Continuous dynamical nodes in straits having arbitrary cross sections, with applications to the Bab-al-Mandab. *J. Phys. Oceanogr.*, **30**, 2515–2534, https://doi.org/10.1175/1520-0485(2000)030<2515:CDMISH>2.0.CO;2.

Raboudi, N. F., B. Ait-El-Fquih, and I. Hoteit, 2018: Ensemble Kalman filtering with one-step-ahead smoothing. *Mon. Wea. Rev.*, **146**, 561–581, https://doi.org/10.1175/MWR-D-17-0175.1.

Racault, M.-F., D. E. Raitsos, M. L. Berumen, R. J. W. Brewin, T. Platt, S. Sathyendranath, and I. Hoteit, 2015: Phytoplankton phenology indices in coral reef ecosystems: Application to ocean-color observations in the Red Sea. *Remote Sens. Environ.*, **160**, 222–234, https://doi.org/10.1016/j.rse.2015.01.019.

Raitsos, D. E., I. Hoteit, P. K. Prihartato, T. Chronis, G. Triantafyllou, and Y. Abualnaja, 2011: Abrupt warming of the Red Sea. *Geophys. Res. Lett.*, **38**, L14601, https://doi.org/10.1029/2011GL047984.

——, Y. Pradhan, R. J. W. Brewin, G. Stenchikov, and I. Hoteit, 2013: Remote sensing the phytoplankton seasonal succession of the Red Sea. *PLOS ONE*, **8**, e64909, https://doi.org/10.1371/journal.pone.0064909.

——, and Coauthors, 2015: Monsoon oscillations regulate fertility of the Red Sea. *Geophys. Res. Lett.*, **42**, 855–862, https://doi.org/10.1002/2014GL062882.

——, R. J. W. Brewin, P. Zhan, D. Dreano, Y. Pradhan, G. B. Nanninga, and I. Hoteit, 2017: Sensing coral reef connectivity pathways from space. *Sci. Rep.*, **7**, 9338, https://doi.org/10.1038/s41598-017-08729-w.

Sathyendranath, S., and Coauthors, 2019: An ocean-colour time series for use in climate studies: The experience of the Ocean-Colour Climate Change Initiative (OC-CCI). *Sensors*, **19**, 4285, https://doi.org/10.3390/s19194285.

Sivareddy, S., H. Toye, P. Zhan, S. Langodan, G. Krokos, O. Knio, and I. Hoteit, 2020: Impact of atmospheric and model physics perturbations on a high-resolution ensemble data assimilation system of the Red Sea. *J. Geophys. Res. Oceans*, **125**, e2019JC015611, https://doi.org/10.1029/2019JC015611.

Skamarock, W. C., and Coauthors, 2019: A description of the Advanced Research WRF version 4. NCAR Tech. Note NCAR/TN-556+STR, 145 pp., https://doi.org/10.5065/1dfh-6p97.

Smeed, D., 1997: Seasonal variation of the flow in the strait of Bab-al-Mandab. *Oceanol. Acta*, **20**, 773–781.

Sofianos, S., and W. E. Johns, 2007: Observations of the summer Red Sea circulation. *J. Geophys. Res.*, **112**, C06025, https://doi.org/10.1029/2006JC003886.

——, and ——, 2015: Water mass formation, overturning circulation, and the exchange of the Red Sea with the adjacent basins. *Red Sea: The Formation, Morphology, Oceanography and Environment of a Young Ocean Basin*, N. Rasul and I. C. F. Stewart, Eds., Springer Earth System Sciences, Springer, 343–353.

Stammer, D., and Coauthors, 2002: The global ocean circulation during 1992–1997, estimated from ocean observations and a general circulation model. *J. Geophys. Res.*, **107**, 3118, https://doi.org/10.1029/2001JC000888.

Sun, R., A. C. Subramanian, A. J. Miller, M. R. Mazloff, I. Hoteit, and B. D. Cornuelle, 2019: SKRIPS v1. 0: A regional coupled ocean-atmosphere modeling framework (MITgcm-WRF) using ESMF/NUOPC, description and preliminary results for the Red Sea. *Geosci. Model Dev.*, **12**, 4221–4244, https://doi.org/10.5194/gmd-12-4221-2019.

Tolman, H. L., 2008: User manual and system documentation of WAVEWATCH-III version 3.14. NOAA/NWS/NCEP/OMB Tech. Note 268, 220 pp., https://polar.ncep.noaa.gov/mmab/papers/tn276/MMAB_276.pdf.

Toye, H., P. Zhan, G. Gopalakrishnan, A. R. Kartadikaria, H. Huang, O. Knio, and I. Hoteit, 2017: Ensemble data assimilation in the Red Sea: Sensitivity to ensemble selection and atmospheric forcing. *Ocean Dyn.*, **67**, 915–933, https://doi.org/10.1007/s10236-017-1064-1.

——, S. Kortas, P. Zhan, and I. Hoteit, 2018: A fault-tolerant HPC scheduler extension for large and operational ensemble data assimilation: Application to the Red Sea. *J. Comput. Sci.*, **27**, 46–56, https://doi.org/10.1016/j.jocs.2018.04.018.

——, S. Sivareddy, N. Raboudi, and I. Hoteit, 2020: A hybrid ensemble adjustment Kalman filter based high-resolution data assimilation system for the Red Sea: Implementation and evaluation. *Quart. J. Roy. Meteor. Soc.*, **146**, 4108–4130, https://doi.org/10.1002/qj.3894.

Triantafyllou, G., F. Yao, G. Petihakis, K. Tsiaras, D. E. Raitsos, and I. Hoteit, 2014: Exploring the Red Sea seasonal ecosystem functioning using a three-dimensional biophysical model. *J. Geophys. Res. Oceans*, **119**, 1791–1811, https://doi.org/10.1002/2013JC009641.

Viswanadhapalli, Y., C. V. Srinivas, S. Langodan, and I. Hoteit, 2016: Predicting extreme rainfall events over Jeddah, Saudi Arabia: Impact of data assimilation with conventional and satellite observations. *Quart. J. Roy. Meteor. Soc.*, **142**, 327–348, https://doi.org/10.1002/qj.2654.

——, H. P. Dasari, S. Langodan, V. S. Challa, and I. Hoteit, 2017: Climatic features of the Red Sea from a regional assimilative model. *Int. J. Climatol.*, **37**, 2563–2581, https://doi.org/10.1002/joc.4865.

——, ——, S. Dwivedi, V. R. Madineni, S. Langodan, and I. Hoteit, 2020: Variability of monsoon low-level jet and associated rainfall over India. *Int. J. Climatol.*, **40**, 1067–1089, https://doi.org/10.1002/joc.6256.

Wang, T., O. P. Le Maître, I. Hoteit, and O. M. Knio, 2016: Path planning in uncertain flow fields using ensemble method. *Ocean Dyn.*, **66**, 1231–1251, https://doi.org/10.1007/s10236-016-0979-2.

Wang, Y., D. E. Raitsos, G. Krokos, J. A. Gittings, P. Zhan, and I. Hoteit, 2019: Physical connectivity simulations reveal dynamic linkages between coral reefs in the southern Red Sea and the Indian Ocean. *Sci. Rep.*, **9**, 16598, https://doi.org/10.1038/s41598-019-53126-0.

Xie, J. S., G. Krokos, S. Sofianos, and I. Hoteit, 2019: Interannual variability of the exchange flow through the strait of Bab-al-Mandeb. *J. Geophys. Res. Oceans*, **124**, 1988–2009, https://doi.org/10.1029/2018JC014478.

Yao, F., and I. Hoteit, 2018: Rapid red sea deep water renewals caused by volcanic eruptions and the north Atlantic oscillation. *Sci. Adv.*, **4**, eaar5637, https://doi.org/10.1126/sciadv.aar5637.

——, ——, L. J. Pratt, A. S. Bower, A. Köhl, G. Gopalakrishnan, and D. Rivas, 2014a: Seasonal overturning circulation in the Red Sea: 2. Winter circulation. *J. Geophys. Res. Oceans*, **119**, 2263–2289, https://doi.org/10.1002/2013JC009331.

——, ——, ——, ——, P. Zhai, A. Köhl, and G. Gopalakrishnan, 2014b: Seasonal overturning circulation in the Red Sea: 1. Model validation and summer circulation. *J. Geophys. Res. Oceans*, **119**, 2238–2262, https://doi.org/10.1002/2013JC009004.

Zhai, P., and A. S. Bower, 2013: The response of the Red Sea to a strong wind jet near the Tokar Gap in summer. *J. Geophys. Res. Oceans*, **118**, 421–434, https://doi.org/10.1029/2012JC008444.

——, ——, W. M. Smlethie Jr., and L. J. Pratt, 2015: Formation and spreading of Red Sea outflow water in the Red Sea. *J. Geophys. Res. Oceans*, **120**, 6542–6563, https://doi.org/10.1002/2015JC010751.

Zhan, P., A. C. Subramanian, F. C. Yao, and I. Hoteit, 2014: Eddies in the Red Sea: A statistical and dynamical study. *J. Geophys. Res. Oceans*, **119**, 3909–3925, https://doi.org/10.1002/2013JC009563.

——, F. Yao, A. R. Kartadikaria, Y. Viswanadhapalli, G. Gopalakrishnan, and I. Hoteit, 2015: Far-field ocean conditions and concentrate discharges modeling along the Saudi coast of the Red Sea. *Intakes and Outfalls for Seawater Reverse-Osmosis Desalination Facilities*, T. M. Missimer, B. Jones, and R. G. Maliva, Eds., Springer, 501–520, https://doi.org/10.1007/978-3-319-13203-7_21.

——, A. C. Subramanian, F. C. Yao, A. R. Kartadikaria, D. Q. Guo, and I. Hoteit, 2016: The eddy kinetic energy budget in the Red Sea. *J. Geophys. Res. Oceans*, **121**, 4732–4747, https://doi.org/10.1002/2015JC011589.

——, G. Gopalakrishnan, A. C. Subramanian, D. Guo, and I. Hoteit, 2018: Sensitivity studies of the Red Sea eddies using adjoint method. *J. Geophys. Res. Oceans*, **123**, 8329–8345, https://doi.org/10.1029/2018JC014531.

——, G. Krokos, D. Guo, and I. Hoteit, 2019: Three-dimensional signature of the Red Sea eddies and eddy-induced transport. *Geophys. Res. Lett.*, **46**, 2167–2177, https://doi.org/10.1029/2018GL081387.

Zodiatis, G., R. Lardner, T. M. Alves, Y. Krestenitis, L. Perivoliotis, S. Sofianos, and K. Spanoudaki, 2019: Oil spill forecasting (prediction). *J. Mar. Res.*, **75**, 923–953, https://doi.org/10.1357/002224017823523982.